The Climatology of Lower Tropospheric Temperature Inversions in China from Radiosonde Measurements: Roles of Black Carbon, Local Meteorology, and Large-Scale Subsidence

JIANPING GUO,[a] XINYAN CHEN,[a] TIANNING SU,[b] LIN LIU,[a] YOUTONG ZHENG,[b] DANDAN CHEN,[a] JIAN LI,[a] HUI XU,[a] YANMIN LV,[a] BINGFANG HE,[c] YUAN LI,[a] XIAO-MING HU,[d] AIJUN DING,[e] AND PANMAO ZHAI[a]

[a] State Key Laboratory of Severe Weather, Chinese Academy of Meteorological Sciences, Beijing, China; [b] Department of Atmospheric and Oceanic Sciences and Earth System Science Interdisciplinary Center, University of Maryland, College Park, College Park, Maryland; [c] Anhui Institute of Meteorological Sciences, Hefei, China; [d] Center for Analysis and Prediction of Storms, University of Oklahoma, Norman, Oklahoma; [e] School of Atmospheric Sciences, Nanjing University, Nanjing, China

ABSTRACT: The variability of the lower tropospheric temperature inversion (TI) across China remains poorly understood. Using seven years' worth of high-resolution radiosonde measurements at 120 sites, we compile the climatology of lower tropospheric TI in terms of frequency, intensity, and depth during the period from 2011 to 2017. The TI generally exhibits strong seasonal and geographic dependencies. Particularly, the TI frequency is found to be high in winter and low in summer, likely due to the strong aerosol radiative effect in winter. The frequency of the surface-based inversion (SBI) exhibits a "west low, east high" pattern at 0800 Beijing time (BJT), which then switches to "west high, east low" at 2000 BJT. Both the summertime SBI and elevated inversion (EI) reach a peak at 0800 BJT and a trough at 1400 BJT. Interestingly, the maximum wintertime EI frequency occurs over Southeast China (SEC) rather than over the North China Plain (NCP), likely attributable to the combination of the heating effect of black carbon (BC) originating from the NCP, along with the strong subsidence and trade inversion in SEC. Correlation analyses between local meteorology and TI indicate that larger lower tropospheric stability (LTS) favors more frequent and stronger TIs, whereas the stronger EI under smaller LTS conditions (unstable atmosphere) is more associated with subsidence rather than BC. Overall, the spatial pattern of the lower tropospheric TI and its variability in China are mainly controlled by three factors: local meteorology, large-scale subsidence, and BC-induced heating. These findings help shed some light on the magnitude, spatial distribution, and underlying mechanisms of the lower tropospheric TI variation in China.

KEYWORDS: Radiosonde observations; Soundings; Climate variability; Seasonal variability

1. Introduction

Meteorological variables have increasingly been recognized as important drivers of the dispersion and dilution of aerosol particles (Wehner and Wiedensohler 2003; Wang et al. 2014; Ding et al. 2016; Guo et al. 2017; Su et al. 2018). The aerosols give feedback to the meteorological conditions mainly through aerosol microphysical effects and radiative effects (Qian et al. 2011; Boucher et al. 2013; Li et al. 2017; Miao et al. 2017a,b; Guo et al. 2018). Such complex interactions between aerosol and meteorological conditions have been extensively studied over the past decades (e.g., Cao et al. 2009; Ding et al. 2016; Li et al. 2017). In particular, much attention has been paid to temperature inversion (TI) and atmospheric stratification within the planetary boundary layer (PBL), which directly affects the dispersion and accumulation of air pollutants (Seidel

et al. 2012; Li et al. 2017). TI is deemed to occur when the temperature increases with altitude, which is generally caused by large-scale subsidence, radiative cooling, and the advection of warm air mass in the PBL (Kahl 1990). TI typically manifests itself as a capping layer on top of the PBL during daytime, limiting the diffusion of atmospheric pollutants and thus favoring the formation of severe air pollution episodes (Stull 1988; Ding et al. 2016; Li et al. 2017; Miao et al. 2017a).

The lower tropospheric TI has been widely recognized as responsible for the enhancement of haze pollution due to the suppression of vertical turbulent mixing in the PBL (Chen and Feng 1995, 2001; Cheng et al. 2007; Johnson et al. 1996; Li et al. 2015; Milionis and Davies 2008). Recent studies have demonstrated that black carbon (BC) is one of the most important light-absorbing aerosol types that modulate TI via the positive aerosol–PBL feedback (Ding et al. 2016; Huang et al. 2018; Wang et al. 2018). For instance, the TI frequency is observed to be positively associated with BC concentrations. However, negligible correlations are found between the TI strength or intensity and BC (Gramsch et al. 2014). Besides, the observational studies at four urban sites in New Zealand in the winter of the period 2010–12 indicate that high TI strength is always associated with high BC emissions (Trompetter et al. 2013). By comparison, the BC below the mixing height has the potential to promote a negative feedback on the atmospheric stability over basin valleys, thereby weakening the ground level TI and

facilitating the dispersal (Ferrero et al. 2014). It seems that the impact of BC on TI is highly dependent on the vertical distribution of BC, which has been comprehensively reviewed by Li et al. (2017).

Additionally, TIs are sometimes found to be located beneath the low-level jet, which is frequently linked to the occurrence of severe storms (Stull 1988; Garreaud and Muñoz 2005; Vihma et al. 2011). These inversions show a loaded-gun upperair sounding pattern, which is occasionally associated with the heavy precipitation (Yan et al. 2019). Also, the TIs have been found to exert a large influence on precipitable water (Tomasi 1977) and atmospheric pollutants (Olofson et al. 2009; Wallace and Kanaroglou 2009a,b). Moreover, TI is an important feature in climate sensitivity; notably, surface-based inversion (SBI) regulates to some extent the variability of sea ice in both hemispheres, thereby exerting positive feedback on albedo (Deser et al. 2010; Kay and Gettelman 2009; Mernild and Liston 2010; Pavelsky et al. 2011).

Depending on the base height of the inversion layer, the TI is typically partitioned into SBIs and elevated inversions (EIs) (Abdul-Wahab et al. 2004). According to their formation mechanisms, TIs are generally classified as radiative inversions, frontal inversions, or subsidence inversions (Ji et al. 2018). Radiative inversions frequently occur at night as the ground surface cools more rapidly than the overlying air (Hyun et al. 2005). Valley inversion is a form of radiative inversion that occurs in valleys and hilly areas (Anquetin et al. 1998). Marine inversion generally occurs in coastal areas and is formed by cool ocean air being blown onto warm land. Frontal inversion tends to develop under the synoptic-scale advection of an air mass, broadly characterized by a weak vertical mixing at the top of the inversion layer by forming a very strong barrier (Zhang et al. 2009). By comparison, subsidence inversion forms when a widespread layer of air descends, which is then compressed and heated as a result of increases in atmospheric pressure. Regardless of the inversion regime, stable stratified inversions have been recognized to suppress the vertical turbulent mixing in the PBL (Ball 1960; Lilly 1968; Stevens 2002; Stevens et al. 2003), resulting in unbalanced surface radiation, increased amounts of atmospheric pollutants, inhibited cloud formation, destruction of surface ozone, and adverse effects on human health (Holzworth 1972; Janhall et al. 2006; Beard et al. 2012; Rendón et al. 2014; Yin et al. 2020).

The TI evolves rapidly on some occasions, which is strongly linked to the diurnal variation of solar radiation reaching the surface, as well as the complex orography (Connolley 1996; Whiteman et al. 1999). In addition, large-scale atmospheric circulation can dramatically affect the occurrence of TI (Bailey et al. 2011). Based on a large number of observations, tremendous progress has been made in quantifying the characteristics of TIs (e.g., frequency, intensity, and depth) at a range of locations around the world that are favorable for the formation of inversions, including the polar regions (Liu and Key 2003; Devasthale et al 2010), the North China Plain (NCP; Xu et al. 2019), central China (Liu et al. 2018), the southern Great Plains (Li et al. 2017), the southwest United States (Bailey et al. 2011), and some major European cities (Kukkonen et al. 2005). However, most of these studies are limited in temporal and spatial coverages. As a result, the explicit large-scale pattern of
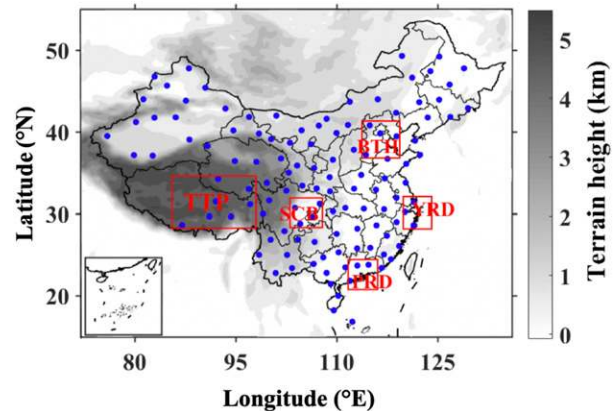

FIG. 1. Spatial distribution of China Radiosonde Network consisting of 120 upper-air sounding sites (blue dots) across mainland China. Also shown are the topography (gray shading) and five regions of interest (ROIs) highlighted in red rectangles, including the Tibetan Plateau (TTP), Sichuan basin (SCB), Yangtze River Delta (YRD), Pearl River Delta (PRD), and Beijing–Tianjin–Hebei (BTH). These ROIs will be used for further analysis of temperature inversions.

TI remains unclear, especially in China. Recently, the spatial and temporal variability of surface inversions have been revealed throughout Europe (Palarz et al. 2018), but this is based on ERA-Interim reanalysis data that are well known to be limited in vertical resolution. The climatology of TI throughout all of China based on high-resolution radiosonde observations have yet to be reported so far.

Since 2011, L-band radiosondes have routinely been launched twice each day at 120 sites forming the China Radiosonde Network (CRN). These provide in situ measurements of the atmosphere at 1.2-s intervals (Guo et al. 2016a; W. Zhang et al. 2018; Guo et al. 2019). The present study uses a 7-yr record (2011–17) of this dataset as the first attempt to elucidate the climatology of TI throughout all of China, with a focus on five regions of interest (highlighted in Fig. 1). Specifically, the large-scale spatial pattern and seasonality of inversions are reported in detail. More importantly, the influential factors are thoroughly investigated in an attempt to provide a reasonable explanation for the observed TI pattern over China.

The remainder of this paper proceeds as follows: section 2 describes the data and methods used in the determination and calculation of SBIs and EIs. The spatial (horizontal and vertical) distributions of inversions are detailed in section 3. Also shown in this section are the diurnal, monthly, and seasonal features of the inversions. The connections of TI pattern are discussed as well with local meteorological variables, largescale subsidence, and BC. Finally, the key findings are summarized in section 4.

2. Data and methods

a. Radiosonde data

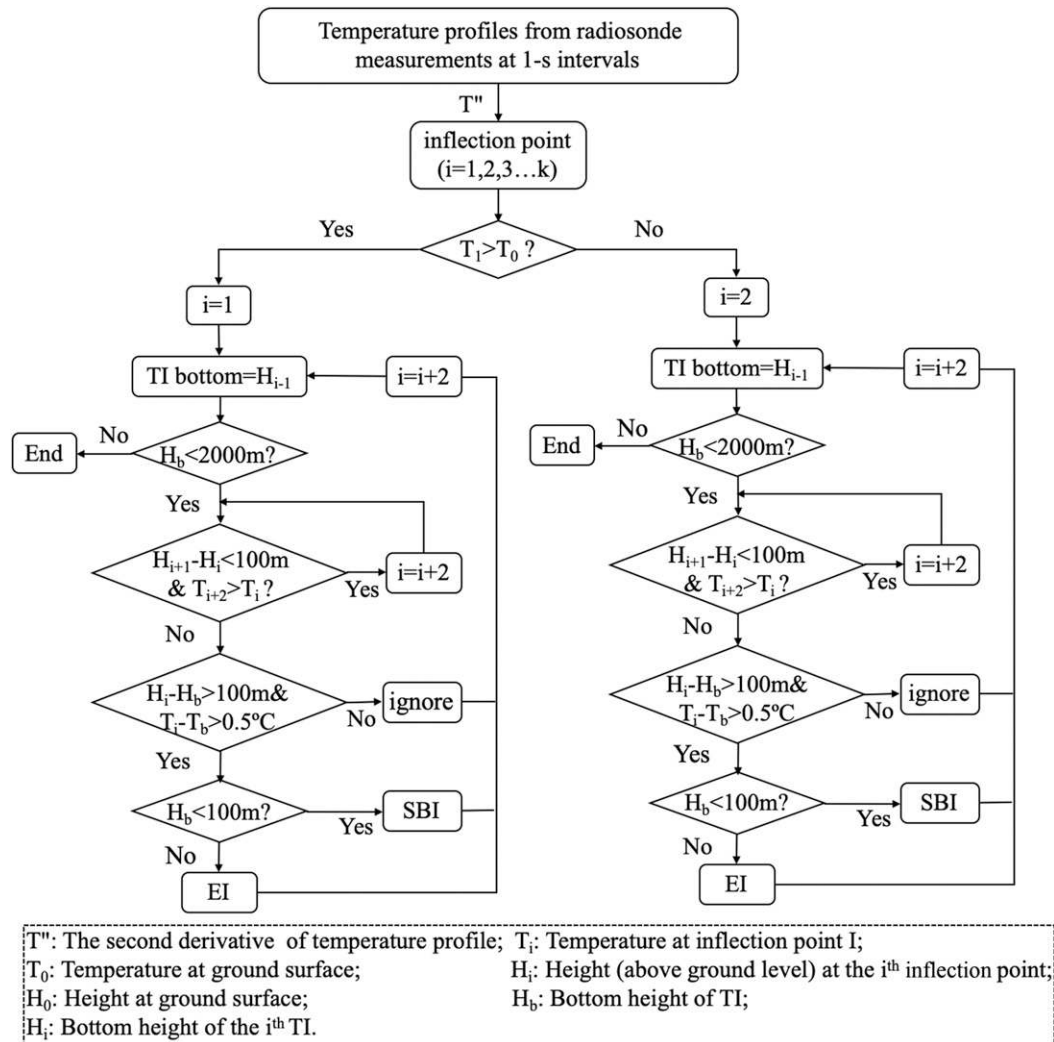Beginning in calendar year 2011, new-generation L-band (1675 MHz) GTS-1 radiosondes have been routinely used at

FIG. 2. Flowchart showing the primary procedures for identifying the SBI and EI using the temperature profiles from 1-s radiosonde measurements. Note that the acronyms have been explained at the bottom.

120 radiosonde stations (Y. Zhang et al. 2018), providing fine-resolution profiles of temperature, pressure, relative humidity, wind speed, and direction at 0800 and 2000 Beijing time (BJT; UTC + 8 h). In the warm season (May through August), additional sounding measurements at most CRN sites are conducted to provide key reference to better predictions of high-impact weather in China, which is significantly influenced by the East Asia summer monsoon (EASM) (Li et al. 2016; Chen et al. 2018). These fine-resolution soundings allow for the characterization of the diurnal variability of inversions in China. These in situ measurements are recorded every 1.2 s, translating to an approximate vertical resolution of 5–8 m. The GTS1 digital radiosonde profiles the atmosphere from the ground surface up to about 30 km above ground level.

Past verification studies (e.g., Bian et al. 2011) indicate that the measurements from the GTS1 radiosonde agree very well with those from Vaisala RS80 radiosonde in the PBL. In

particular, the accuracy of the temperature profile has been found to be less than 0.1 K in the troposphere (Tao et al. 2006; Ma et al. 2011). Therefore, these radiosonde measurements have been widely used in a variety of applications, including detection of the cloud base (Y. Zhang et al. 2018) and estimation of the PBL height (Guo et al. 2016b; Su et al. 2017; Zhang et al. 2016; W. Zhang et al. 2018). Therefore, the radiosonde measurements from the CRN are considered of sufficient quality to determine the features of inversions throughout China.

The topography and geomorphology throughout China vary greatly, including coastal regions, basins, plains, deserts, mountainous areas, and plateaus; this variation arguably affects the occurrence and intensity of inversions (Fast et al. 1996; Whiteman et al. 1996). The severe haze pollution caused by increasing anthropogenic activities in eastern China is another driving force for the variability of TIs (Guo
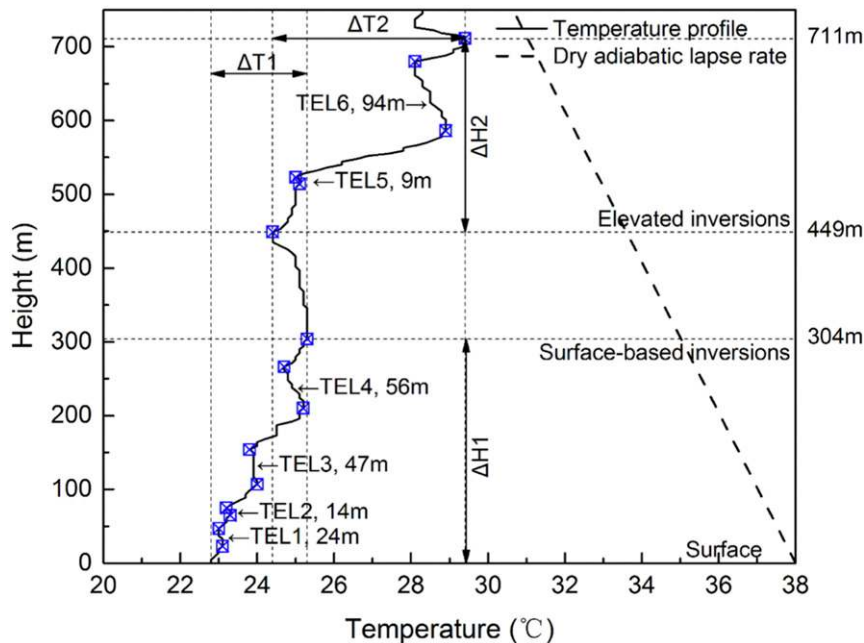
FIG. 3. Sample temperature profile (black curve) from the Xingtai (114.5°N, 37.07°E) upper-air sounding site at 2000 BJT 28 Jul 2016 showing how to define a surface-based inversion (SBI) and elevated inversion (EI), in addition to the depths (ΔH1, ΔH2) and strength (ΔT1/ΔH1, ΔT2/ΔH2). The blue square indicates the turning point of temperature profile. Thin embedded noninversion layers (TEL; temperature decreases with altitude) and their corresponding depth are indicated in black text. The bold dotted line indicates dry adiabatic lapse rate.

et al. 2011; Li et al. 2017; Liu et al. 2018; Yang et al. 2018). Therefore, five regions of interest (ROIs) are selected for further in-depth investigations of TIs in an attempt to better elucidate the mechanism of inversion formation: 1) the Tibetan Plateau (TTP), 2) Sichuan Basin (SCB), 3) Yangtze River Delta (YRD), 4) Pearl River Delta (PRD), and 5) Beijing–Tianjin–Hebei (BTH). Further details of these five ROIs are provided in Table S1 in the online supplemental material.

b. Black carbon and reanalysis dataset

Because large-scale BC observations are still lacking in China, here we use the Modern-Era Retrospective Analysis for Research and Application version 2 (MERRA-2) reanalysis, which is NASA's new-generation reanalysis produced by the Goddard Earth Observing System, version 5 (GEOS-5). GEOS-5 is a state-of-the-art system that couples a global atmospheric general circulation model (GEOS-5 AGCM) to the National Centers for Environmental Prediction (NCEP) Grid-point Statistical Interpolation (GSI) analysis (Rienecker et al. 2011). The BC total column extinction (i.e., optical depth) is publicly available from the MERRA-2 aerosol diagnostics. Recent validation efforts suggest that the BC total extinction data from the MERRA-2 reanalysis agree well with ground- or satellite-based observations, albeit with some deficiencies due to the missing BC emissions (Buchard et al. 2017).

Furthermore, several meteorological variables have been utilized such as wind speed and wind direction at 10 m above

ground level (AGL), 2-m surface air temperature (Ts), and the potential temperature at both 700 hPa and the surface level, all of which are obtained from the MERRA-2 reanalysis in order to perform a causal analysis with regard to inversions. The LTS was calculated as the difference in potential temperature between 700 hPa and the surface (Slingo 1987) and was able to adequately describe the thermodynamic state of the lower troposphere (Guo et al. 2016a). This MERRA-2 reanalysis has been intensively evaluated in previous studies, which shows that it can well reproduce the near-surface wind fields (Gelaro et al. 2017; Rienecker et al. 2011; Coy et al. 2016). In terms of the performance of the 850-hPa wind fields from MERRA-2 reanalysis in China, previous quantitative validation analyses have proved well the robustness of MERRA-2 in adequately capturing the wintertime prevailing wind across China (R. H. Zhang et al. 2019).

c. Classification of temperature inversions

Based on the fine-resolution temperature soundings from the CRN described in section 2a, TIs can first be identified using the first-derivative algorithm developed by Kahl (1990) and Serreze et al. (1992). The major procedures undertaken are outlined as follows. First, a series of derivatives for one given temperature profile is calculated, resulting in a profile of derivatives. Then, this derivative profile is scanned upward from the surface to the 2000-m level; an inversion layer is identified when the derivative is positive and remains positive
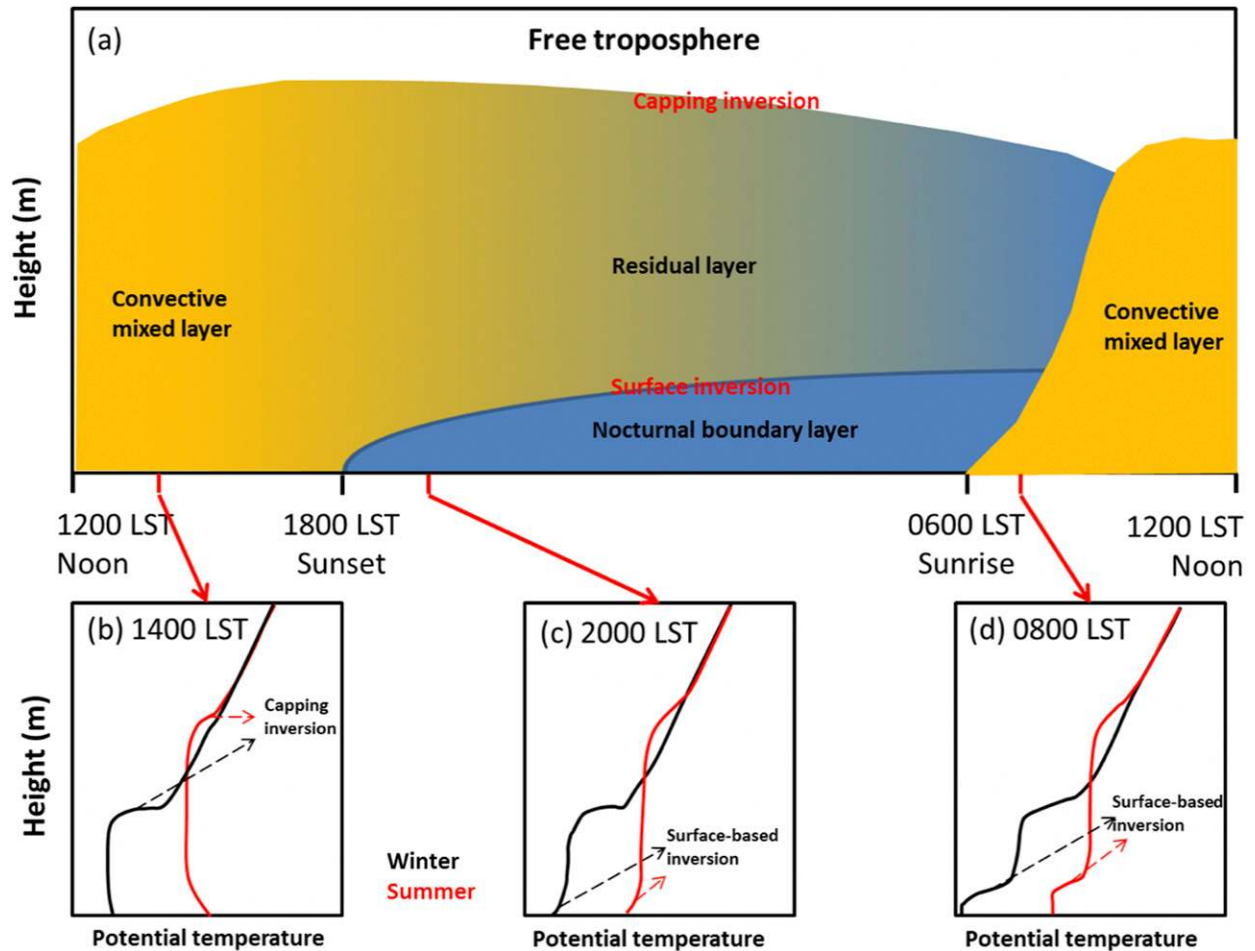
FIG. 4. Schematic diagram illustrating the typical diurnal cycle of boundary layer and temperature inversions over land, (a) adapted from Stull (1988), and (b)–(d) corresponding to the potential temperature profile at 1400, 2000, and 0800 LST, respectively. For highlighting the distinction of the low-atmosphere inversions between winter and summer, the free-atmosphere potential temperature profiles (the overlapping parts between black and red lines) are assumed to be identical for these two seasons.

over an altitude range of at least 100 m. The temperature difference between the top and base of the inversion is required to be greater than 0.5°C. Very thin negative derivative layers are occasionally encountered. If these layers are less than 100 m, they are considered to be one embedded part of an inversion layer. In this way, a number of inversion layers are identified and further classified into SBIs and EIs. The SBIs represent those inversions with bases below a height of 100 m AGL, whereas the EIs are inversions with bases above 100 m. Unless otherwise noted, all TIs are deemed to have a base height below a height of 2000 m AGL. The flowchart is schematically shown in Fig. 2.

For each sounding that contains an inversion layer, the following three parameters are calculated: 1) inversion depth, which denotes the difference in altitude between the top and the base of the inversion (ΔZ); 2) inversion intensity, which represents the temperature difference across the inversion layer divided by the inversion depth ($\Delta T/\Delta Z$); and 3)

inversion frequency, calculated as the number of profiles with an inversion divided by the total number of profiles. The same calculations were performed for both SBIs and EIs.

Figure 3 schematically shows how EIs and SBIs were identified. It can be seen that four thin embedded-noninversion layers (TELs), each less than 100 m, were embedded in the SBI layer. Thus, they can be regarded as one part of the entire inversion layer below 304 m AGL. The EIs were identified between the bottom (449 m) and top (711 m), with two TELs. Consequently, SBI intensity was determined to be 0.82°C $(100\,\text{m})^{-1}$, which was much weaker than the EI intensity $[1.91°C\ (100\,\text{m})^{-1}]$.

d. Conceptual framework

Figure 4 is a schematic diagram that describes the conceptual framework used to facilitate the understanding of the temporal evolution of low-level inversion layers from the thermodynamic perspective, based on a typical clear-sky PBL
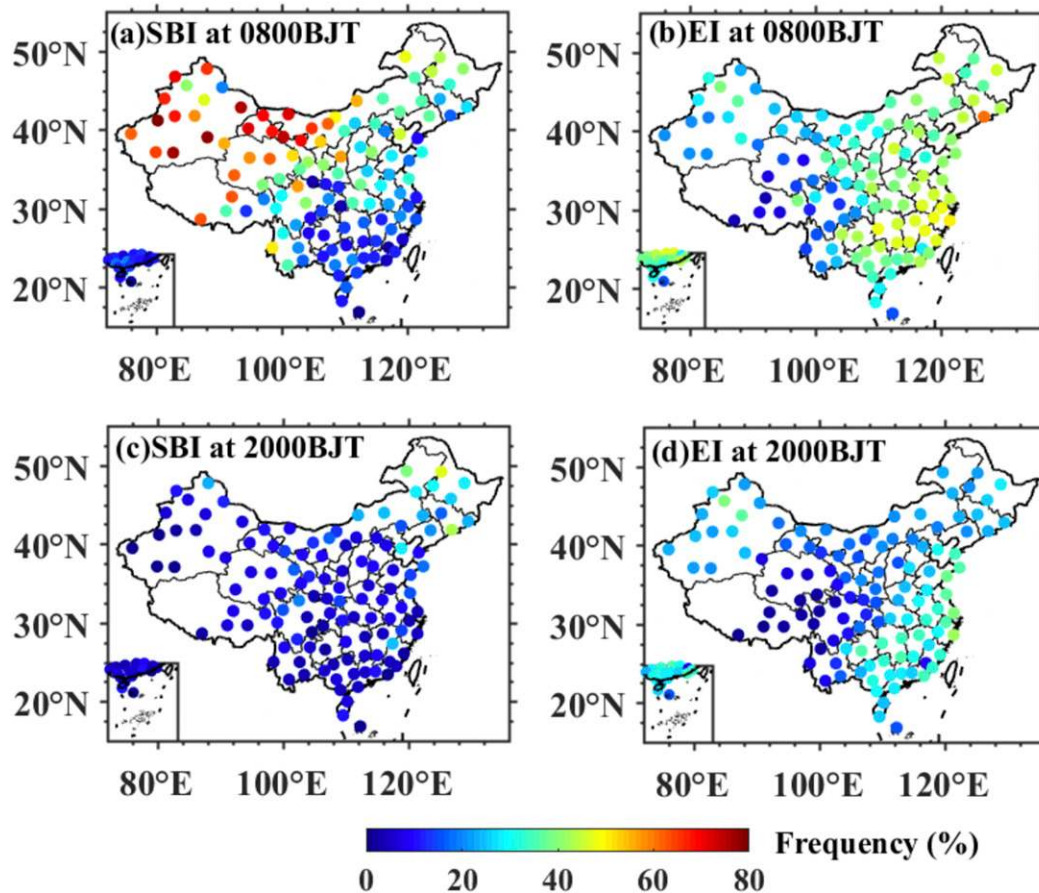
Fig. 5. Spatial distributions of the annual mean frequency of (left) SBI and (right) EI at (a),(b) 0800 and (c),(d) 2000 BJT across China, which are derived from high-resolution radiosonde measurements for the period 2011 to 2017.

over flat land. For simplicity, the effects of thermal advection were ignored. This idealization was necessary to identify the essential processes governing the formation and evolution of inversion layers, which could be used as theoretical guidance

for the statistical analysis of inversions from radiosonde measurements.

During the night, the radiative cooling of the land surface is generally stronger than that of the overlying air (Petty 2006).
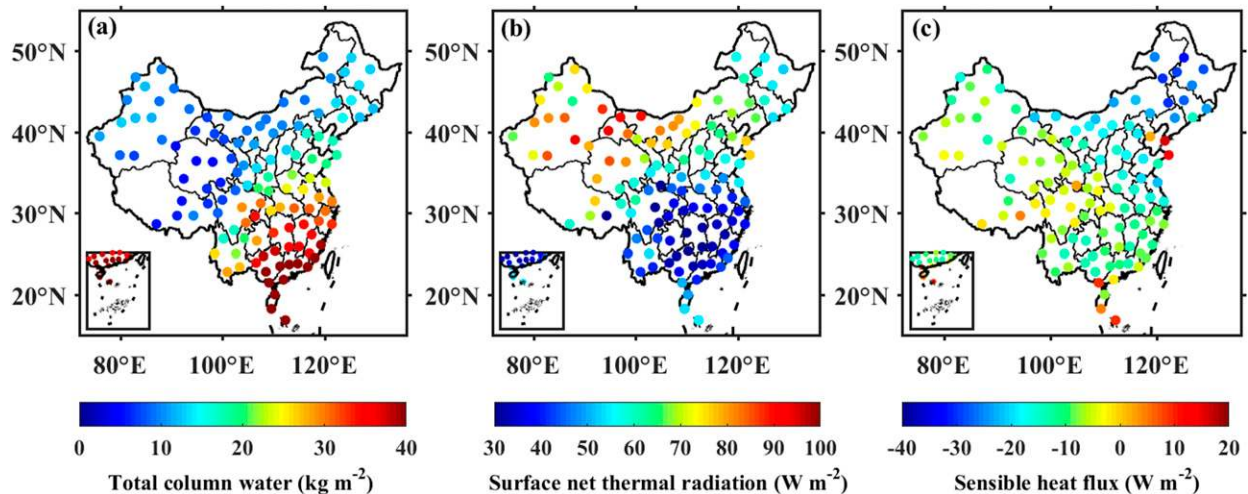

Fig. 6. Spatial distributions of the (a) annual mean total column water, (b) surface net thermal radiation, and (c) sensible heat flux at night (2000–2300 BJT) for the period from 1 Jan 2015 to 31 Dec 2015. The data are obtained from ERA-Interim reanalysis.
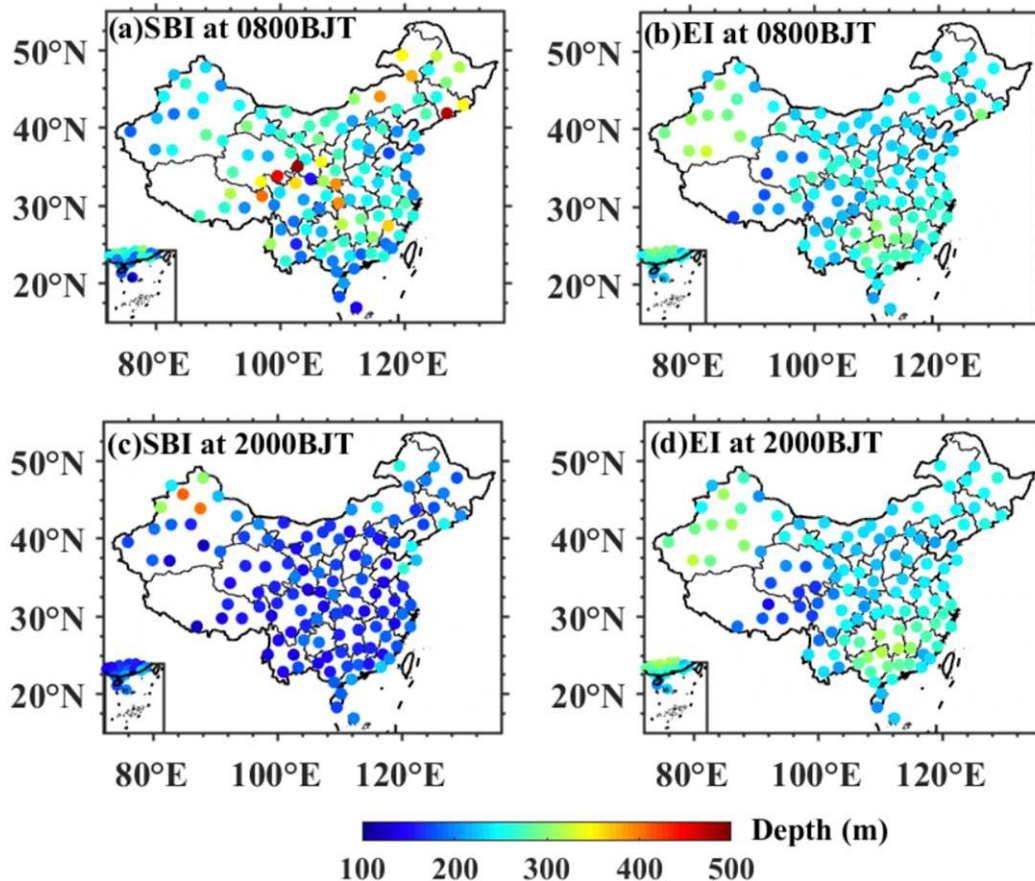
FIG. 7. As in Fig. 5, but for annual mean depth of SBI and EI.

This differential longwave cooling leads to the formation of a surface inversion layer (Fig. 4c). After sunrise, incoming solar radiation heats the land surface, generating convective turbulence and building up a surface mixed layer. The mixing erodes the nocturnal surface inversion layer (Stull 1988). This process can be considered as the transition of turbulent kinetic energy (TKE) to the potential energy of the fluid of the mean atmosphere (Stevens 2007). The erosion rate is controlled by the intensity of surface buoyancy fluxes because stronger surface buoyancy fluxes increase the TKE that destabilizes the PBL, and ultimately erodes the nocturnal surface inversion. Therefore, in summer when the surface heating is strong, after-dawn surface inversions should occur much less frequently and also be less intense than those in winter (Fig. 4d).

As the surface heating continues, the surface mixed layer deepens and penetrates into the residual layer that is typically capped by a weak inversion. In summer when the surface buoyancy fluxes are strong and cause a mixed layer, which further rapidly elevates the capping inversion that develops over the heated underlying surface during daytime due to the positive buoyancy flux from the ground. This stratified TI layer acts as a lid to the buoyant thermals originating from the convectively mixed layer, leading to frequent observed EI (red curve in Fig. 4b). By comparison, in winter the capping inversion should remain stronger due to the lack of convective penetration (black curve in Fig. 4b). The capping inversion will persist, as the upper boundary of the residual layer, until it is eroded by the convective activities of the next day.

3. Results and discussion

a. Spatial distribution of SBIs and EIs and the potential impact of topography and land cover

Figure 5 shows the geographic distributions of the annual average frequencies of SBIs and EIs at 0800 and 2000 BJT, respectively. Overall, both inversion metrics occur more frequently at 0800 BJT, which confirms the conceptual model presented in Fig. 4. Interestingly, more than half of the soundings experience SBI episodes across almost all sites over northwest China at 0800 BJT. In contrast, less frequent SBI episodes dominate Northeast China. This "west high, east low" pattern of SBI frequency could be due to a time lag of 1–2 h between BJT and local standard time (LST). For example, the radiosonde balloons launched at 0800 BJT in western China generally correspond to 0600 or 0700 LST when the sun typically does not rise on the eastern horizon, especially in winter. If we neglect the horizontal advection of potential temperature, the atmospheric cooling near the surface at night is mainly
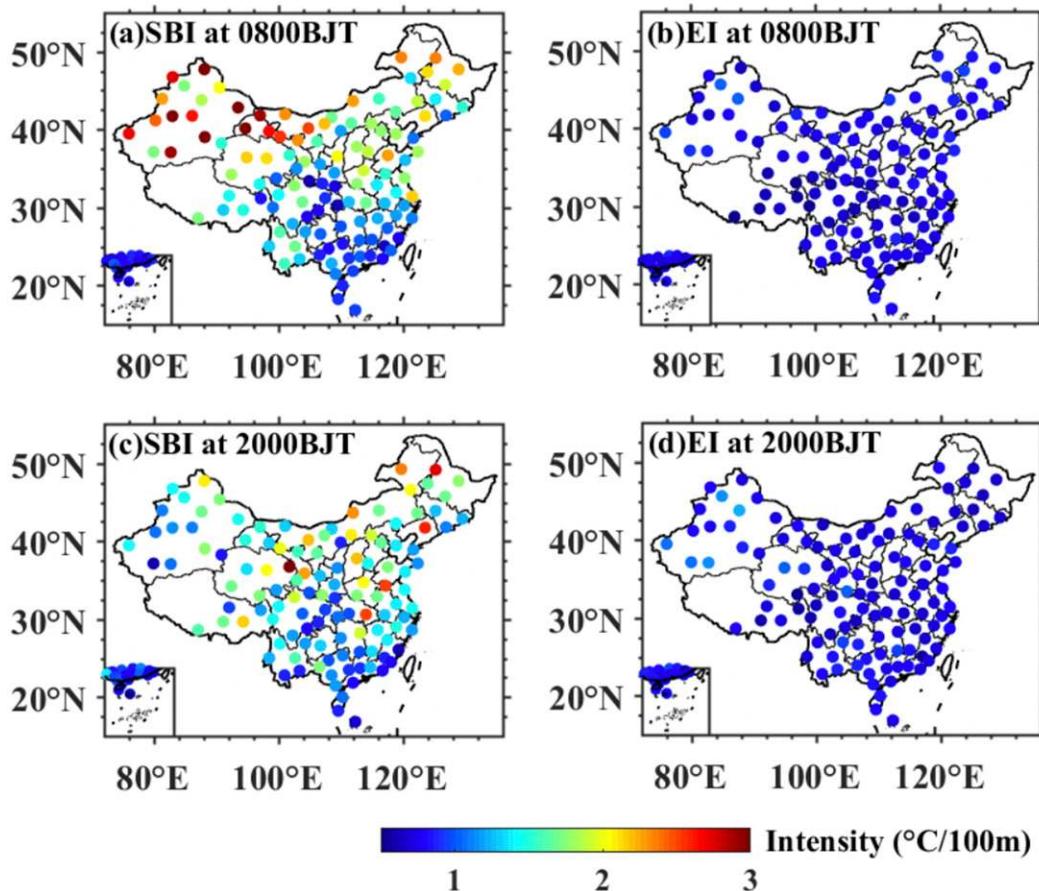
FIG. 8. As in Fig. 5, but for annual mean intensity of SBI and EI.

controlled by sensible heat flux divergence and the net long-wave radiative flux divergence (Steeneveld et al. 2010). As shown in Fig. 6, the distribution of surface net thermal radiation is broadly consistent with that of SBI frequency at 0800 BJT. As compared to that in eastern China (low-lying region), the drier atmosphere in western China tends to cause larger positive net longwave radiation flux during night, thereby resulting in a much faster drop in land surface temperature in western China. This in turn leads to a larger radiative cooling rate near the surface, which could be the dominant driving factor accounting for the frequent formation of SBI in western China at 0800 BJT (Wang et al. 2016). Given the spatial pattern of negative sensible heat flux (Fig. 6c), which is not similar to that of SBI frequency in Fig. 5, sensible heat flux could only be a secondary cause, if any, for the spatial discrepancy observed in SBI frequency.

However, the EI frequency at 0800 BJT and 2000 BJT does not exhibit the west high, east low pattern like SBI frequency. Interestingly, the EIs occur more frequently in East China than in West China, both in the morning and the evening (Figs. 5b,d).

As shown in Fig. 7, the annual average depth of TI ranges from 100 to 500 m. The SBI layer at 0800 BJT is on average deeper than that at 2000 BJT. The depths of both types of inversion at 0800 BJT are spatially heterogeneous across mainland China, indicating strong geographic dependence of SBI in the morning. In contrast, the mean depths of EIs at 2000 BJT in most parts of China are slightly shallower, compared with those at 0800 BJT, and there is no noticeable difference between the morning and the evening EI depths. More interestingly, the EI intensity is significantly less than the SBI intensity both in the morning and the evening (Fig. 8). It is also noteworthy that the spatial pattern of SBI intensity at 2000 BJT seems not uniform throughout China, with relatively low intensity at northwestern China and southern China.

Owing to their strong impacts on the temperature profile in the lower PBL, topography and land use and land cover, among other factors, have to be considered in an attempt to better explain the spatial pattern of SBI. As shown in Fig. 9a, all of the mean SBI frequency at 0800 BJT has a positive correlation with elevation, regardless of the season. By comparison, the SBI frequency at 2000 BJT is found to positively correlate with elevation except in winter (Fig. 9b). It is well known that the terrain in China exhibits a pronounced west high, east low pattern. It would be expected that the stations at western China (generally with high elevation) tend to
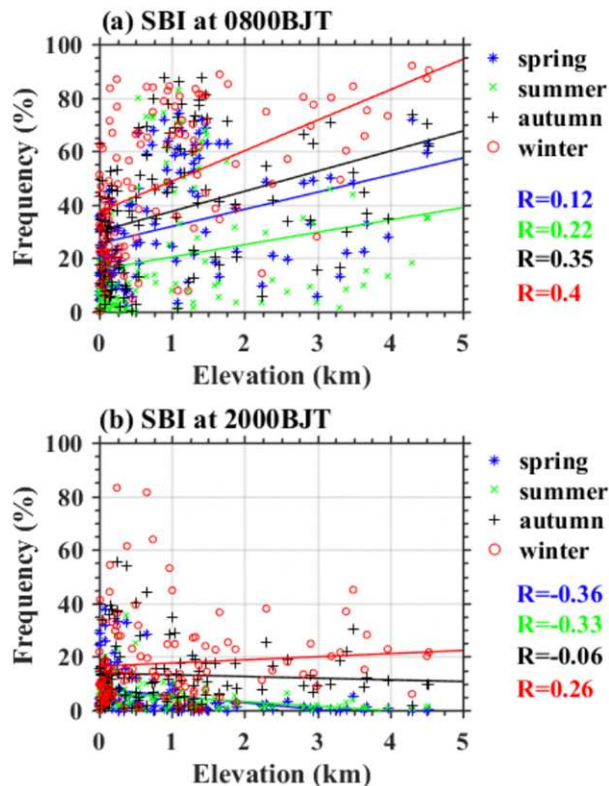
FIG. 9. Seasonal mean SBI frequency shown as a function of elevation at (a) 0800 and (b) 2000 BJT. Also indicated are the correlation coefficients (*R*) between SBI frequency and elevation. Note that each point (various shape) in the scatterplots represents the data pair for each station.

experience more SBI, compared with those in eastern China, because of the much earlier LST in the morning. This positive correlation between SBI frequency and elevation would most likely be caused by the time lag of radiosonde launching. Additionally, Figs. 6a and 6b show that the large radiative cooling coincidently corresponds to low humidity over high-altitude region, which favors the formation of SBI over western China at 0800 BJT (Fig. 5a). This leads to a certain connection between SBI frequency in the early morning and elevation or terrain. However, it remains challenging to quantify the dependence of SBI frequency on elevation. Furthermore, a close-up look at those stations with an elevation less than 500 m indicates that the points are much scattered (Fig. 9a). As a matter of fact, these low-lying stations are mostly limited to eastern China (to the east of 110°E), and thus we argue that the dependence of SBI frequency on elevation is also weak even in regions without delay of local time to launch balloons. Similarly, the dependence of EI frequency at 2000 BJT on elevation seems to be weak as well (Fig. 9b).

As illustrated in Fig. 10, the seasonal SBI frequency varies dramatically for a given type of land cover for both 0800 and 2000 BJT, especially for the land covers classified as "grasslands," "croplands," "urban and built-up lands," and "barren." At 0800 BJT, the SBI occurs 0.16% of the time over

urban and built-up lands in the autumn, whereas the most SBI (91.95%) occurs over grassland in the winter. In terms of the dependence of SBI occurrence on land cover, apparently it is not significant either, as evidenced by the large variability of frequency range (from 18% to 83%) for any given land cover. Therefore, land cover could not be the major driver of the spatial variability of TI.

b. Diurnal and seasonal variations of temperature inversion

Figure 11 illustrates the seasonally averaged height-resolved frequencies of both types of inversion during the period from 2011 to 2017. Overall, the occurrence frequency of temperature inversions at 2000 BJT does not exceed 20% in the PBL (0–2 km), regardless of the season or type of inversion. In comparison, TIs at 0800 BJT are present less than 50% of the time throughout the PBL.

Both types of inversion are most commonly observed in winter, followed by autumn, spring, and the least in summer, particularly near the ground surface. There are two reasons for the wintertime maximum TI frequency: 1) the ground surface in the Northern Hemisphere receives the least solar insolation in winter due to that season having the lowest solar elevation angle of the year, and 2) the atmosphere is typically driest in winter (Kassomenos et al. 2014; Nodzu et al. 2006), resulting in stronger longwave cooling during the morning and night (Zheng et al. 2019).

In the vertical direction, the layer closer to the ground surface experiences more frequent SBIs (Figs. 11e–h) than EIs (Figs. 11i–l). This could be owning to the different criteria used to define SBIs and EIs, with SBI requiring that the base height of TI should be less than 100 m above ground level. Three soundings per day (0800, 1400, and 2000 BJT) are launched in summer at most sites of the CRN, which allows us to characterize the temporal variation of height-resolved inversion frequency during the course of a day. The diurnal cycle of atmospheric structure within the PBL is strongly driven by solar radiation (Stull 1988). Thus, the diurnal variation in TIs tends to reflect pronounced signals from solar radiation; this is detailed in the conceptual framework in section 2d. Irrespective of the season, the TIs occur most frequently at 0800 BJT. This was because inversions are more likely to occur when radiative cooling occurred in the early morning. The surface longwave cooling accumulates throughout the night, leading to a build-up and strengthening of surface-level inversions in the morning. It is noteworthy that SBIs are least frequent at 1400 BJT throughout the PBL in summer, with the exception of some sporadic EI episodes in the upper levels of the PBL (Fig. 11j). This indicates that inversions in the summer afternoon periods are limited to the upper levels of the PBL, which could be due to warm air masses or light-absorbing aerosols. The EIs in the early evening (2000 BJT) and early morning (0800 BJT) are more frequent throughout the PBL in winter than in summer (Figs. 11i–l). In winter, the net outgoing infrared radiation generally exceeds the incoming solar radiation especially in the early morning, leading to a negative radiative imbalance and a positive temperature gradient upward in the vertical. This is largely responsible for the relatively high frequency of TI in winter compared to summer when this
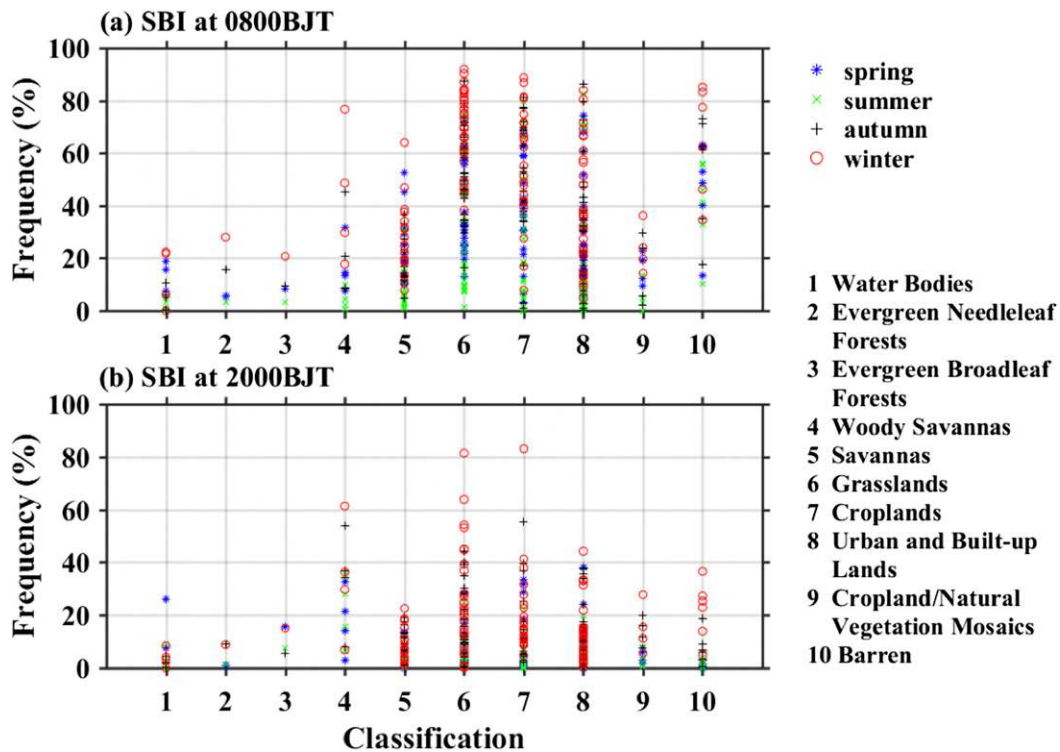
FIG. 10. Seasonal SBI frequency shown as a function of land cover at (a) 0800 and (b) 2000 BJT. The land cover data were obtained from the Land Cover Type Yearly Climate Modeling Grid (CMG; https://ladsweb.modaps.eosdis.nasa.gov/missions-and-measurements/products/MCD12C1).

imbalance is either weak or positive (Devasthale et al. 2010), which helps maintain a strong inversion. In addition, most EI episodes at 0800 BJT occur at approximately 0.3 km AGL, except in winter, whereas the highest EI frequency at 2000 BJT occurs at heights ranging from 1 to 2 km AGL, except in summer.

The spatial distribution of seasonal mean SBI frequency is shown in Fig. 12. On average, the SBI has a maximum frequency at 0800 BJT in winter, especially in both West and Northeast China, followed by autumn, spring, and the minimum in summer. Such a salient seasonal contrast, however, cannot be observed at 2000 BJT.

Similarly, the seasonally averaged SBI depth at 0800 BJT is much greater than at 2000 BJT (see Fig. S1 in the online supplemental information), with the maximum SBI depth occurring in winter. It is known that radiative cooling generally peaks in the morning and in the boreal winter, which tends to lead to a thickening of the inversion layer (André and Mahrt 1982). At both 0800 and 2000 BJT, the average depths of EIs are lowest in summer, as shown in Fig. S2. Compared with the spatial distribution of the SBI depth, the distribution of the EI depth is much more spatially homogeneous and uniform. In addition, the EI shows the maximum depth in winter, with no apparent difference between morning and evening.

As shown in Fig. S3, the SBI intensity in the morning is on average stronger than in the evening, regardless of the season.

In terms of the seasonal variability in inversion intensity, both types of inversion are weaker in summer (Figs. S3 and S4). Interestingly, the spatial patterns of the EI intensity at 0800 and 2000 BJT for all seasons are much more uniform than the SBI intensity. This indicates that EIs are less susceptible to ground surface due to the indirect contact with the ground surface.

c. Potential impact of large-scale circulation and BC on wintertime EI frequency

Figure 13 shows the spatial distributions of EI frequencies at 0800 BJT for spring, summer, autumn, and winter. At 2000 BJT, the spatial pattern of the EI frequency bears a striking resemblance to that at 0800 BJT, albeit with a much smaller magnitude (Fig. 14). Unlike the spatial pattern of SBI frequencies (Figs. 12a–d), in western China (including the TTP) there is not a high EI frequency in the early morning, whereas a much larger EI frequency is observed at radiosonde sites across eastern China. The EI frequency over eastern China is generally much higher than that over western China, except in winter and summer. The EI frequency is much higher in the early morning (0800 BJT) than in the early evening (2000 BJT) in all seasons (Figs. 13 and 14). The lowest and most uniform spatial pattern of EI frequency is observed to occur in summer, which could be connected to the unstable atmospheric conditions induced by the EASM (Ding 1994). Conversely, the spatial pattern in winter is characterized by the highest and most
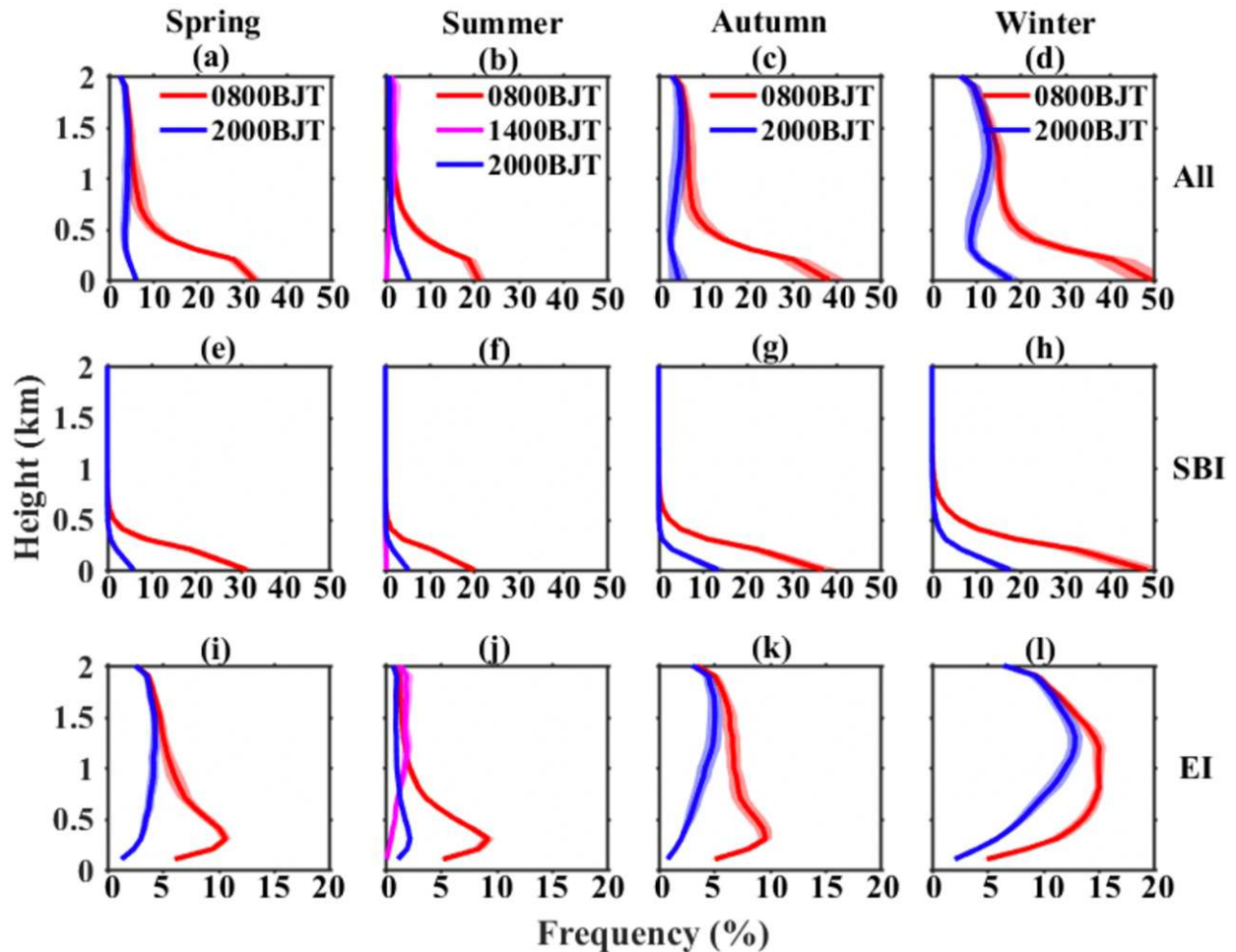
FIG. 11. Height-resolved frequency of temperature inversion below 2000 m averaged over all radiosonde stations in China for the period 2011–17 for (top) all inversions, (middle) SBI, and (bottom) EI, respectively. The columns denote the results in (a),(e),(i) spring [March–May (MAM)], (b),(f),(j) summer [June–August (JJA)], (c),(g),(k) autumn [September–November (SON)], and (d),(h),(l) winter [December–February (DJF)]. The color-shaded areas represent the 95% confidence interval ($\bar{x} \pm 1.96\sigma/n$).

heterogeneous EI frequency across China. Interestingly, the maximum wintertime EI frequency occurs over Southeast China rather than over NCP, while the relatively smaller wintertime EI frequency occurs over the NCP.

A subsidence inversion is generally produced by the adiabatic warming of an air mass when a sinking motion occurs. As shown in Fig. 15, the subsidence inversion arising from the Siberian high is relatively stronger (notably at 925 hPa) in winter over Southeast China, compared with the NCP. This spatial pattern roughly agrees with that of the EI frequency. On top of that, it appears that the warm and moist air mass at 850 hPa originating from the East China Sea is advected over the continent of mainland China. As such, a reversal of the normal behavior of the moisture profile occurs, typically termed "moisture inversion," in which a layer of cool and dry air at the surface is overlain by a layer of warm and moist air. The atmospheric levels with moisture inversion are generally expected to experience warming due to the heat release caused

by condensation of extra water vapor. Figure 16 further indicates that the warm advection in association with southerly winds over southern China at 850 hPa, combined with the northerly winds near the surface in the mean-state, contribute to the high frequent EI observed over Southeast China. Additionally, the dominant widespread motion occurs in subtropical anticyclones, where the subsiding air parcels meet a surface flow of warm maritime air (Figs. 15 and 16). As a result, the trade wind inversion formed over Southeast China. Putting these factors together, this indicates that both sinking motions associated with Siberian highs from the northwest and trade wind inversions originating from the northwestern Pacific play nonnegligible roles in accounting for the high frequent wintertime EI events exclusively found in Southeast China.

Also noteworthy is that there exists large interannual variability of EI frequency in winter in eastern China, no matter whether in the morning or in the evening, which is clearly illustrated in Fig. S4. This intermittent appearance of the EIs
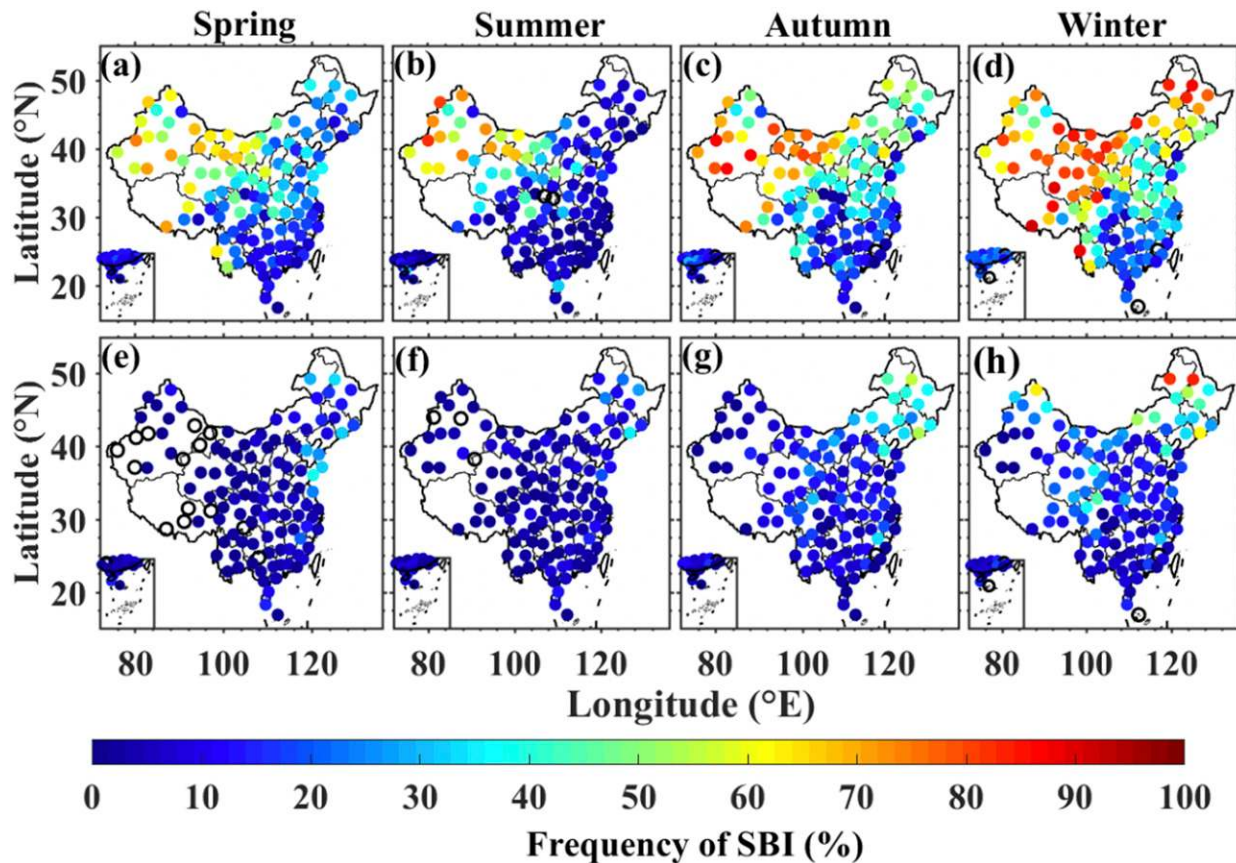
FIG. 12. Spatial distributions of the seasonal mean frequency of SBI at (top) 0800 and (bottom) 2000 BJT in (a),(e) spring, (b),(f) summer, (c),(g) autumn, and (d),(h) winter. The hollow black circle indicates that no inversion has been detected.

found in eastern China is most likely modulated by the large interannual variability of the South China Sea winter circulation (Wang et al. 2020) and the strength of the East Asian winter monsoon, both of which are largely influenced by the processes linked to the sea surface temperature anomaly over the tropical Pacific (Chen et al. 2000, 2020).

d. Potential impact of BC on wintertime EI frequency

In addition to the impact of large-scale subsidence on EI, BC is another important factor. It is well recognized that BC, the most important light-absorbing aerosol, is able to affect the temperature profiles. The warming effect induced by the BC highly depended on the altitude where the BC resides (Li et al. 2017). In the following paragraphs, we will mainly discuss the potential BC-induced radiative impact on the spatial discrepancy of wintertime EI frequency, since it is widely believed that additional aerosol emissions, especially BC, are produced due to winter heating over the NCP (e.g., Xiao et al. 2015). Figure 13d shows that the prevailing northerly or northeasterly winds tend to bring BC particles emitted from northern or northeastern China, the largest emission source region, to southeastern China. The transboundary transport of BC causes large amounts of BC to be suspended in the upper PBL or lower troposphere (Y. Zhang et al. 2019). These additional BC

particles absorb the solar radiation, and at the same time reduce the solar radiation reaching the ground surface (Ding et al. 2016; Huang et al. 2018). This would warm the atmosphere at upper PBL or lower troposphere but cool the air near the surface, which leads to the inadvertent formation of EIs over Southeast China. Furthermore, the formation of EIs prevents the vertical dissipation of atmospheric pollutants and thus enhances the BC concentration in PBL. Such interactions between BC and temperature inversions have been previously reported at several places in China based on field observations (e.g., Li et al. 2015). Recent studies (e.g., Wang et al. 2018) suggest that the radiative effect of BC has a strong dome effect in rural areas, especially in the areas downwind of the high BC emission regions. Figures 13 and 14 illustrate that most parts of northwestern China experience relatively high frequencies of EIs at 0800 and 2000 BJT in winter, which is likely related to the relatively high BC emissions (Cao et al. 2006). Therefore, we speculate that the radiative forcing of BC could contribute to the formation and intensification of SBI and EI episodes, to some extent.

It is noticeable that the total extinction of BC is considerably higher over the NCP compared with South China in summer when southerly winds prevail, resulting in a higher EI frequency over North China, even though there are high levels of
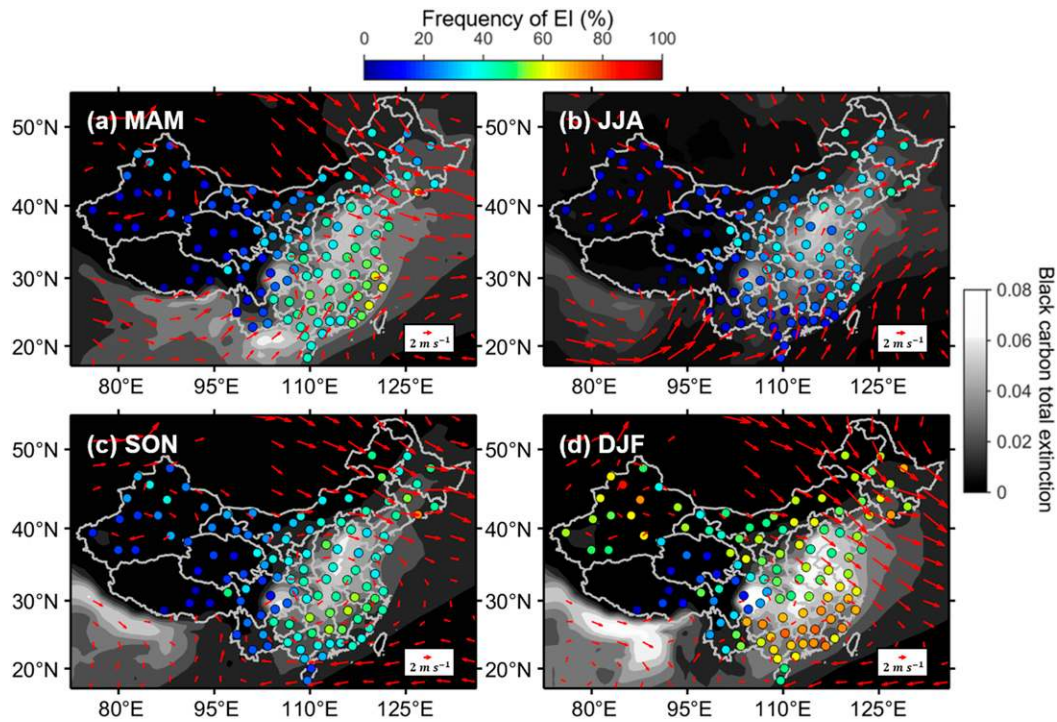
FIG. 13. The black carbon total extinction (colored areas) and wind vector fields at the 850-hPa pressure level (arrows), overlaid with seasonal mean frequency of EI (color-shaded dots) at 0800 BJT during the (a) spring (MAM), (b) summer (JJA), (c) autumn (SON), and (d) winter (DJF) seasons for the period 2011–17. For clarification, the wind speeds below 2 m s^{-1} are exaggerated to 2 m s^{-1}.
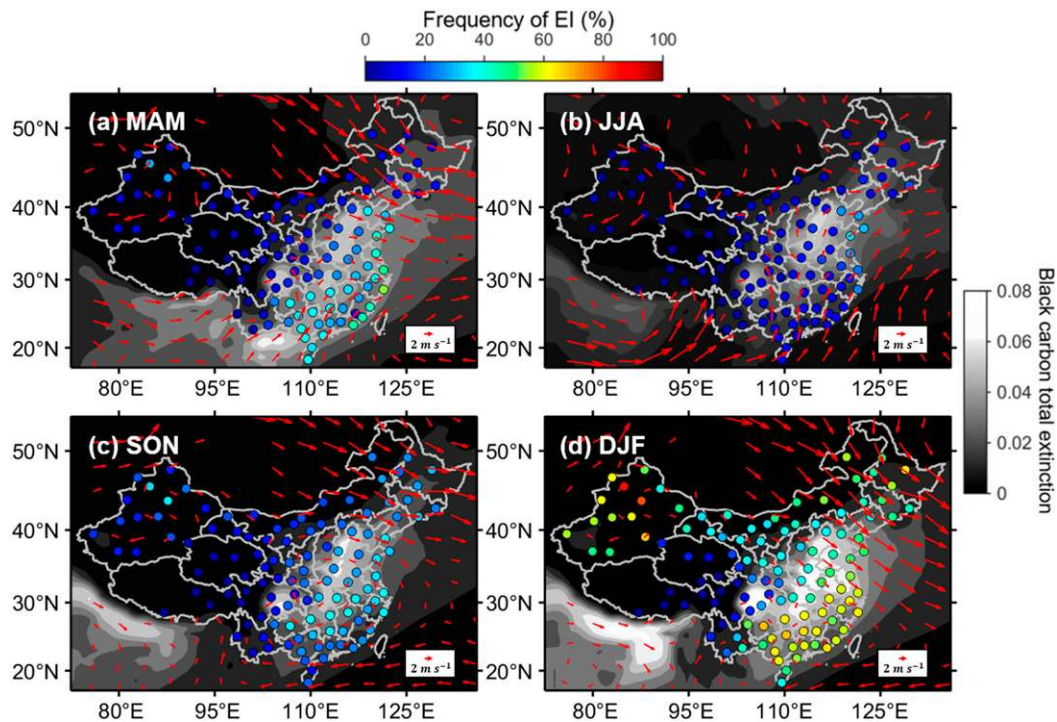
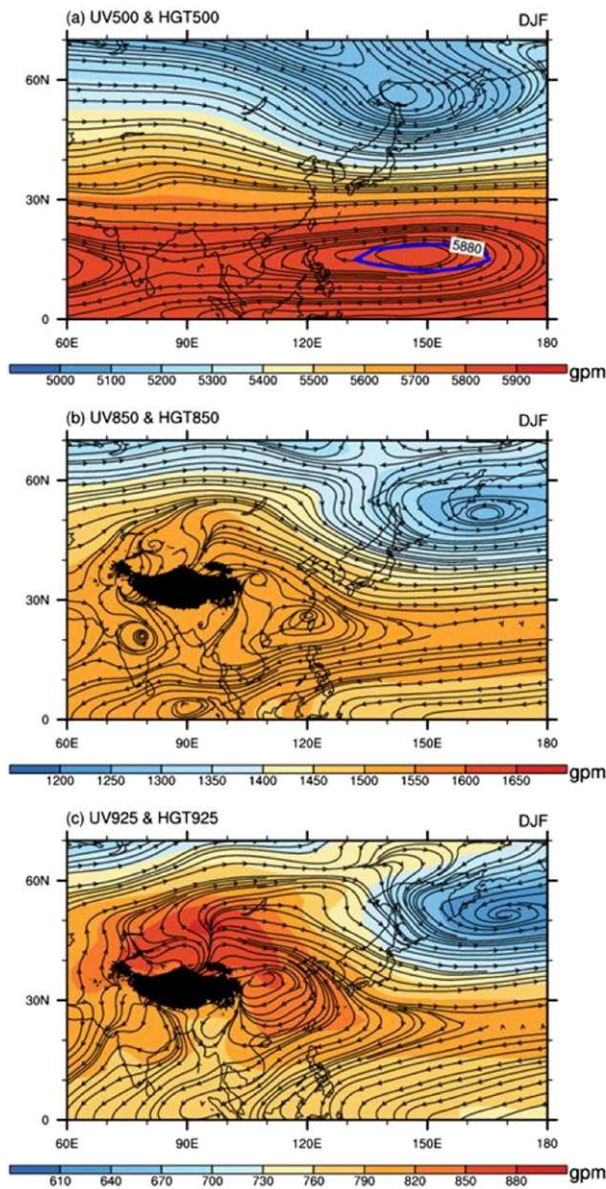FIG. 14. As in Fig. 13, but for EI frequency at 2000 BJT.

FIG. 15. The climatological mean winds (given as streamlines) superimposed over the geopotential height (given as shaded colors) at (a) 500, (b) 850, and (c) 925 hPa during winter (DJF) for the period 2011–17. The meteorological data are obtained from the NCEP–NCAR reanalysis dataset. The black shaded areas denote those regions with an elevation greater than 3000 m.

precipitation scavenging during summer across all of eastern China. Combining the spatial pattern of EI frequency at 0800 and 2000 BJT reveals that the effect of prevailing wind patterns is significant in regulating the EI frequency.

The seasonal averaged EI intensity is weaker than that of SBIs (see Figs. S3 and S4). In the morning in spring and summer, the EI intensity in Northeast China is slightly higher than in other regions. In the evening, the EI intensity in Northwest China is slightly higher than in other regions. In autumn and winter, there are no significant differences in the EI intensity over China in either the morning or evening (Fig. S5).

Previous observational studies indicate that BC could cool the ground surface but cause a heating effect in the lower troposphere during wintertime over China (Ding et al. 2016; Su et al. 2020; Zhao et al. 2020). To illustrate how transboundary transport BC affects the formation of EI in a straightforward way, we obtain the vertical distribution of BC mass concentration from an airplane in Beijing on 11 December 2016 (Fig. 17), in which the BC mostly resides in the middle to upper part of PBL. To figure out how the BC affects the atmosphere in the PBL, we show the profiles of temperature on the same days from simultaneously measured radiosonde and MERRA-2 reanalysis (Fig. 17). On the whole, the MERRA-2 captures well the temperature profile in this case given the high consistency starting from the surface to upper parts of PBL and even beyond. It is worth noting that there exists an elevated layer of high BC concentration near the top of PBL observed on 11 December 2016. Coincidentally, the temperature profiles from both sounding and reanalysis reveal the significant EI episodes occurring therein. More importantly, the prevailing southerly winds would bring a large amount of BC from the southern part of Hebei province, a major source region of anthropogenic aerosols (including BC). Therefore, this lends credence to the observational evidence that transboundary transported BC could possibly enhance the frequency of EI. This corroborates our findings revealed from Fig. 13d. However, the EI observed here could not totally rule out the influence by the warm-air advection from south, which would lead to inversion as well. To achieve a more robust signal of the effect of long-range transported BC on EI, five other cases with vertical measurements of BC in Beijing in December of 2016 are presented in Fig. S6. Unfortunately, we could not see any signals of EI, let alone the BC impact on EI. Therefore, the experiments are highly warranted to accomplish this challenging task in the future.

In addition, the relationships are analyzed between SBI intensity, EI intensity, LTS and BC (Fig. S7). At 0800 BJT, high concentrations of BC tend to occur when the inversion intensity is relatively weak [less than $2°C$ $(100 \text{ m})^{-1}$] and the lower troposphere is stable (LTS ranging from 20 to 35 K). What is more interesting is that at night, the BC concentration tends to reach its peak under both low and high TI intensity conditions, indicating that the BC relates to neither SBIs nor EIs. In particular, when the atmosphere was extremely unstable (with lowest LTS), the total extinction of BC appears not to change much with EI intensity, either in the morning or the evening. In this case, the aforementioned subsidence or advection inversion likely overrides the inversion that is induced by BC.

e. Regional characteristics of temperature inversions

In terms of the national average, the occurrence frequencies of EI and SBI at 0800 BJT are almost similar to each other throughout the year but are much higher than their corresponding frequencies at 2000 BJT, especially in winter (Fig. 18a). Another striking feature is that the SBI at 2000 BJT
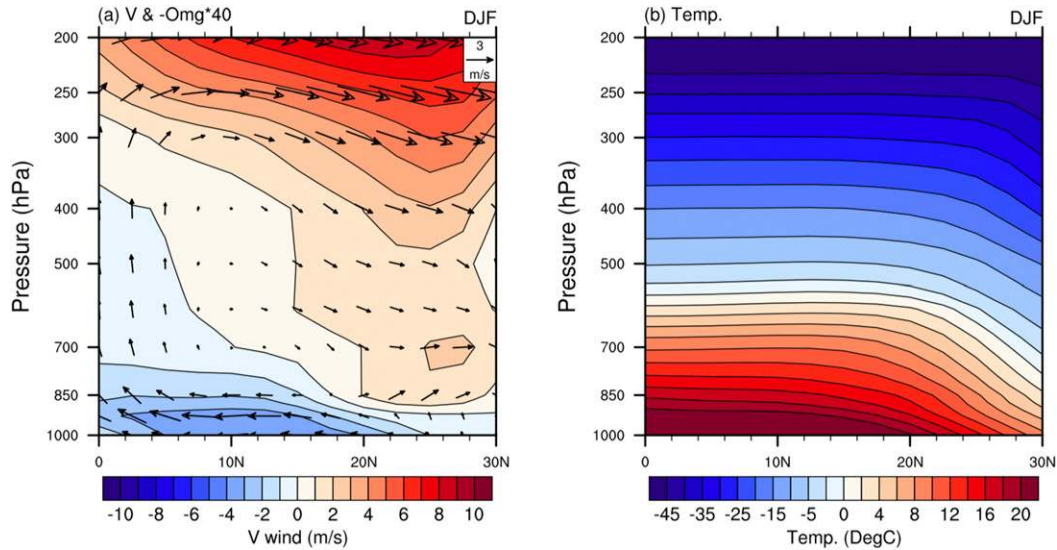
FIG. 16. Pressure–latitude cross sections of (a) meridional wind (shading; m s^{-1}) and vertical velocity (vectors; 0.025 Pa s^{-1}), and (b) temperature averaged from 100° to 120°E during winter (DJF) for the period 2011 to 2017.

is dramatically shallower than others except for summer (Fig. 18b). Interestingly, the SBI intensity is much stronger than EI intensity throughout the year, irrespective of in the morning or evening. The intensity of SBI reaches more than 2°C (100 m)$^{-1}$ in December and January, which is more than twice the intensity of EI. To better understand the regional features of inversions, five ROIs (Fig. 1), each of which has received increasing attention in recent years due to the joint influences of global warming and air pollution, are further analyzed. Figure 19 shows the regional average frequency,

depth, and intensity of SBIs on a monthly basis over the ROIs. The SBI frequency in the evening (2000 BJT) in each ROI is significantly lower than in the morning (0800 BJT) in all months (Fig. 19a). Geographically speaking, the SBI frequency reaches the maximum in the morning over the TTP, with minima over the YRD and PRD. However, the TTP has almost no inversions in the early evening from February to August. The BTH experiences the much more frequent SBI episodes in all seasons except for summer, compared with SCB, YRD, and PRD. This is in sharp contrast to the regional differences in EI frequency (Figs. 20a,d).
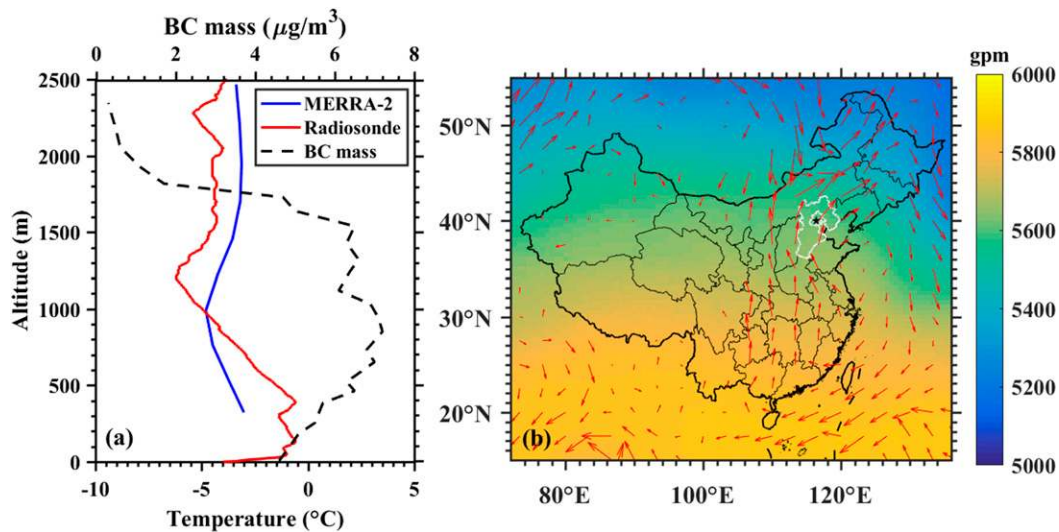

FIG. 17. (a) Vertical profiles of temperature from MERRA-2 (in blue) and radiosonde measurements (in red), as compared with the simultaneously BC vertical distribution as measured by aircraft (black dashed line) in Beijing on 11 Dec 2016. (b) The wind fields at 850 hPa superimposed by 500-hPa geopotential height on the same day as in (a). Note that the solid black star denotes the location of the radiosonde station and black carbon observation in Beijing, and the thick white lines indicate the boundaries of Beijing and Hebei province.
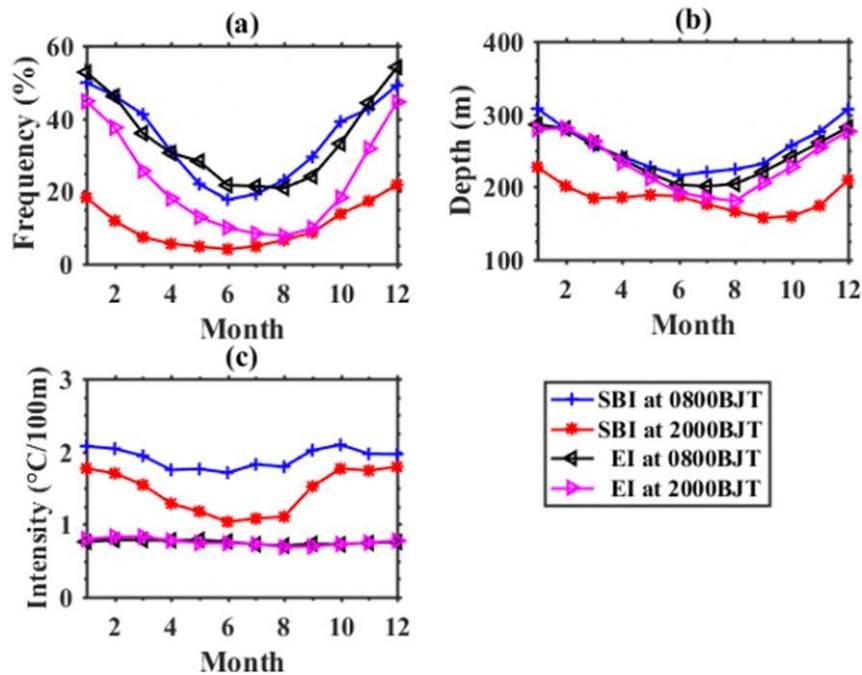
FIG. 18. National mean (a) frequency, (b) depth, and (c) intensity of temperature inversion derived from high-resolution radiosonde measurements during the period 2011–17.

Besides, the intensity of SBI is found to be much stronger in the morning over BTH, compared with other ROIs (Figs. 19c,f).

Except over the TTP, the inversion depth in the ROIs is similar in all months in the morning (Fig. 19b), suggesting that there is no apparent seasonal dependence in SBI depth. In the early evening, the SBI depth over BTH reaches a peak in May, whereas the smallest depth occurs in winter (Fig. 19e), in sharp contrast to the seasonality of the SBI frequency. For the TTP,
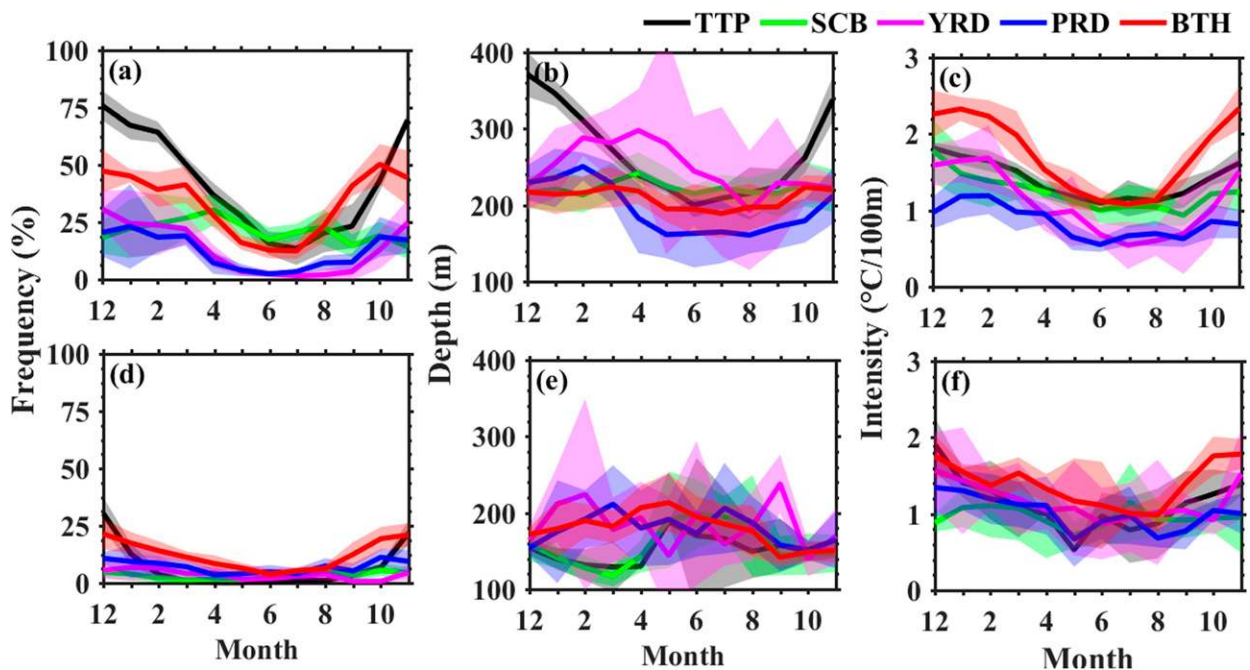

FIG. 19. The average (a),(d) frequency, (b),(e) depth, and (c),(f) intensity of SBI in each ROI as a function of month shown for (top) 0800 and (bottom) 2000 BJT. Note that the color-shaded areas represent one standard deviation of mean inversion frequency.
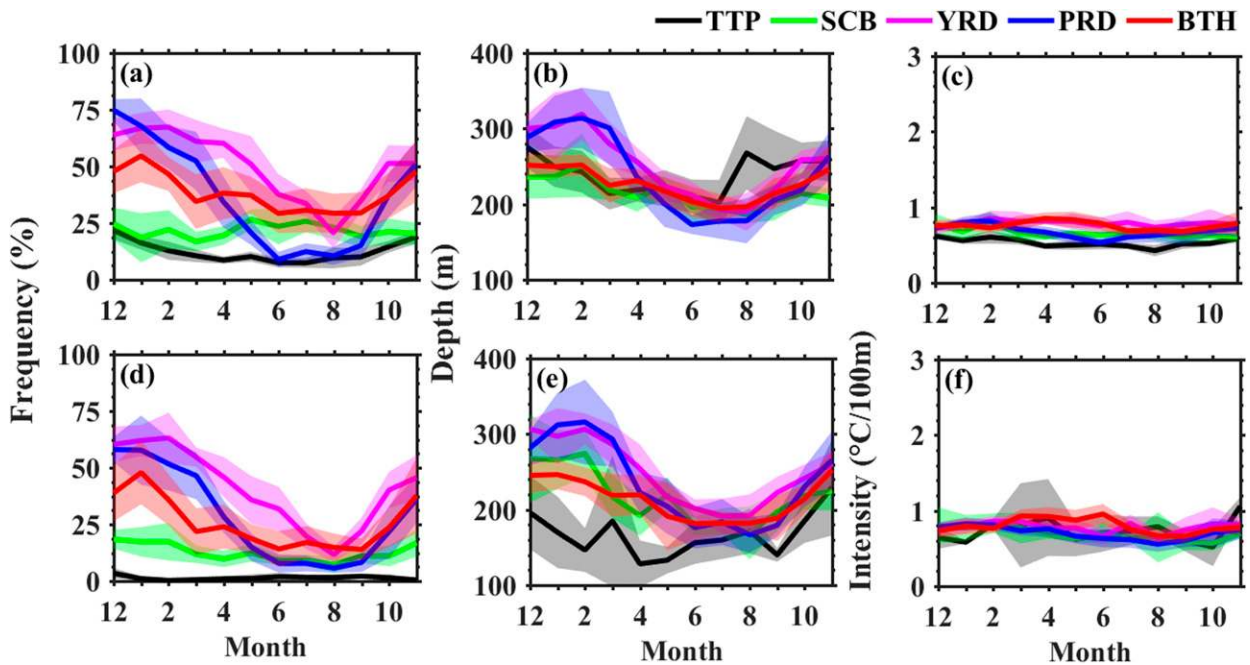
FIG. 20. As in Fig. 19, but for EI.

the inversion depth (both SBI and EI) at 0800 BJT exhibits similar seasonal variability to the inversion frequency, with the minima observed in June. By comparison, the depth over the BTH peaks in May at 2000 BJT. At 0800 BJT, the inversion intensity over BTH is slightly larger than in the TTP or SCB, whereas the weakest inversion intensity occurs in the YRD and PRD. At 2000 BJT (Fig. 19f), there is no significant difference in the SBI intensity in these five ROIs.

As shown in Figs. 19 and 20, the EI frequency at 0800 and 2000 BJT over the TTP is much lower than the SBI frequency, particularly in winter, possibly due to the scarcity of horizontal advection and large-scale subsidence. Except over the BTH, the EI frequency in the other ROIs is much more than the SBI frequency in all months (Fig. 20). The same spatial discrepancy in the EI depth in the morning and evening is apparent in all ROIs, with the exception of TTP, where the EI depth is slightly lower than in the other ROIs at 2000 BJT. The EI intensity over the TTP at 0800 BJT is much smaller than in the other ROIs (Fig. 20).

f. Potential influences of local meteorology

Several meteorological variables that may affect temperature inversions are further analyzed here, including Ts, 10-m wind speed (WS), and LTS. To investigate the influence of these meteorological variables across China, we analyze the spatial pattern of correlation between inversion intensity and meteorological variables. As illustrated in Fig. 21, the spatial distribution of correlation coefficient (R) between inversion intensity and three meteorological variables does not exhibit uniform positive or negative signs across China, regardless of the TI types. The correlation is the strongest for SBI intensity and LTS ($R = 0.24$), followed by SBI intensity and Ts ($R = -0.18$), SBI intensity and WS ($R = -0.07$), EI intensity

and WS ($R = 0.06$), EI intensity and LTS ($R = 0.06$), and the weakest correlation ($R = -0.04$) for EI intensity and Ts. Therefore, the meteorological variables, by and large, are more closely associated with SBI intensity than with EI intensity. In particular, wind speed and SBI intensity have an inverse relationship ($R = -0.07$), as do surface temperature and SBI intensity ($R = -0.18$), but a positive correlation is found between the SBI intensity and LTS ($R = 0.24$). This indicates that a stable PBL, low temperature, and weak wind speed combine to favor the intensification of SBIs in China, which is in good agreement with the well-established relationships between these factors identified in previous studies (e.g., Nygård et al. 2017). Conversely, the wind speed is positively correlated with the EI intensity ($R = 0.06$).

To obtain a holistic understanding of the impact of meteorological variables on the SBI and EI intensities, the 2D joint probability distributions are explicitly checked of LTS, wind speed, and surface temperature versus inversion frequency and intensity, respectively (Figs. 22 and 23). Overall, a greater LTS generally corresponds to a higher frequency and stronger intensity of inversions, particularly within a suitable range of wind speeds and surface temperatures (Fig. 22). This could be due to the greater LTS values representing a more stable PBL, which in turn facilitates the formation of TI in the PBL. When the lower troposphere is extremely unstable (LTS < 10 K), it is difficult to find out the influence of wind speed on the SBI and EI frequency and is impossible for both SBI and EI to frequently occur. Conversely, when the PBL is thermodynamically stable in the vertical direction (LTS > 30 K), a high SBI frequency is closely associated with relatively low surface temperature (Fig. 22c). By comparison, a more disorderly pattern is observed for the joint dependence of EI frequency on
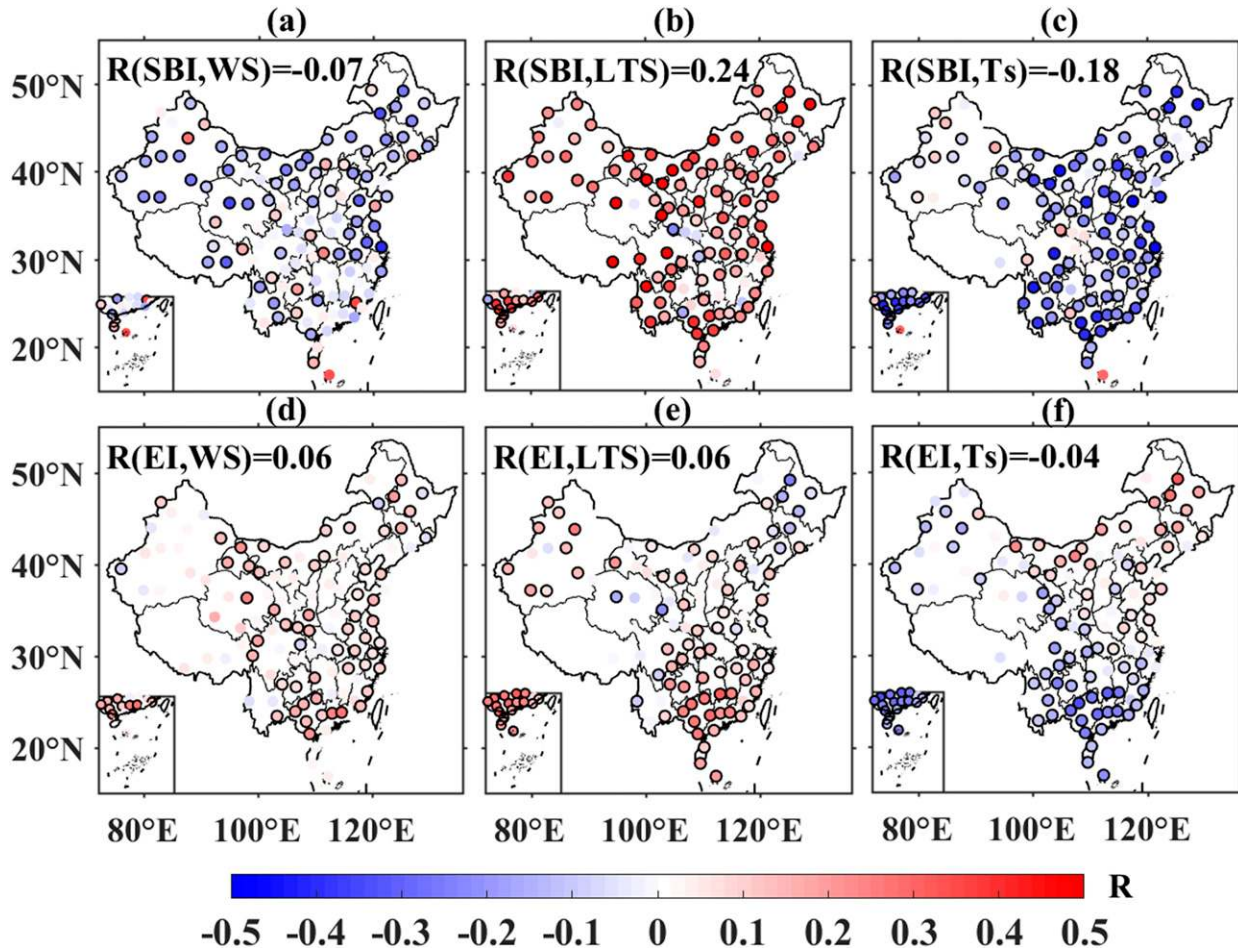
FIG. 21. Spatial distribution of correlation coefficients (R) between inversion intensity of (top) SBI or (bottom) EI and (a) 10-m wind speed (WS), (b) lower tropospheric stability (LTS) and (c) 2-m surface air temperature (Ts). Note that all these meteorological variables are obtained from MERRA-2 reanalysis. Color-shading dots outlined in black indicate that R values are statistically significant ($p < 0.05$), and the mean R is given for each panel.

both LTS and wind speed, given the scattering of hot spots in Fig. 22b. Overall, the SBI and EI frequency decrease as the surface temperature increases, implying that the surface temperature anticorrelates with inversion frequency. This broadly agrees with the correlation distribution shown in Figs. 21c and 21f.

Figure 23 shows the combined effect of these meteorological variables on the inversion intensity. Similar to the inversion frequency, the 10-m wind speed has almost no effect on the SBI intensity when the lower troposphere is unstable, considering the almost invariant SBI intensity with respect to the wind speed shown in Fig. 23a. When the LTS is large enough (approximately 35 K), the SBI intensity tends to be the strongest under wind conditions ranging from 5 to 9 m s^{-1} (Fig. 23a). The 10-m wind speed seems much larger than that in the previous modeling (Lüpkes et al. 2008) and observational (Cassano et al. 2016; Riordan 1977) studies, in which the strongest SBI inversions are observed to occur when the wind speed is 2–6 m s^{-1}. By comparison, the EI intensity tends to be stronger under high wind conditions, particularly for those cases with

LTS between 10 and 35 K, or under low wind conditions (<3 m s^{-1}) combined with extremely stable PBL (LTS > 35 K), as shown in Fig. 23b. Interestingly, the SBI intensity under relatively stable PBL conditions (LTS > 10 K) generally increases as the surface temperature decreases (Fig. 23c), which is broadly consistent with the results of Connolley (1996). Figure 23d shows no apparent dependence of EI intensity on surface temperature, indicating little effect of surface temperature on the EI intensity. This sounds reasonable in that the EI is supposed to be less susceptible to the influence of land surface than SBI. Therefore, the dependence of TI intensity (especially the EI intensity) on local meteorology in the PBL exists exclusively under limited restricted conditions.

4. Conclusions

The dataset of lower tropospheric temperature inversions (TIs) in China is seldom reported in previous studies due to the lack of long-term high-resolution radiosonde measurements, which considerably impairs our understanding of PBL. In this
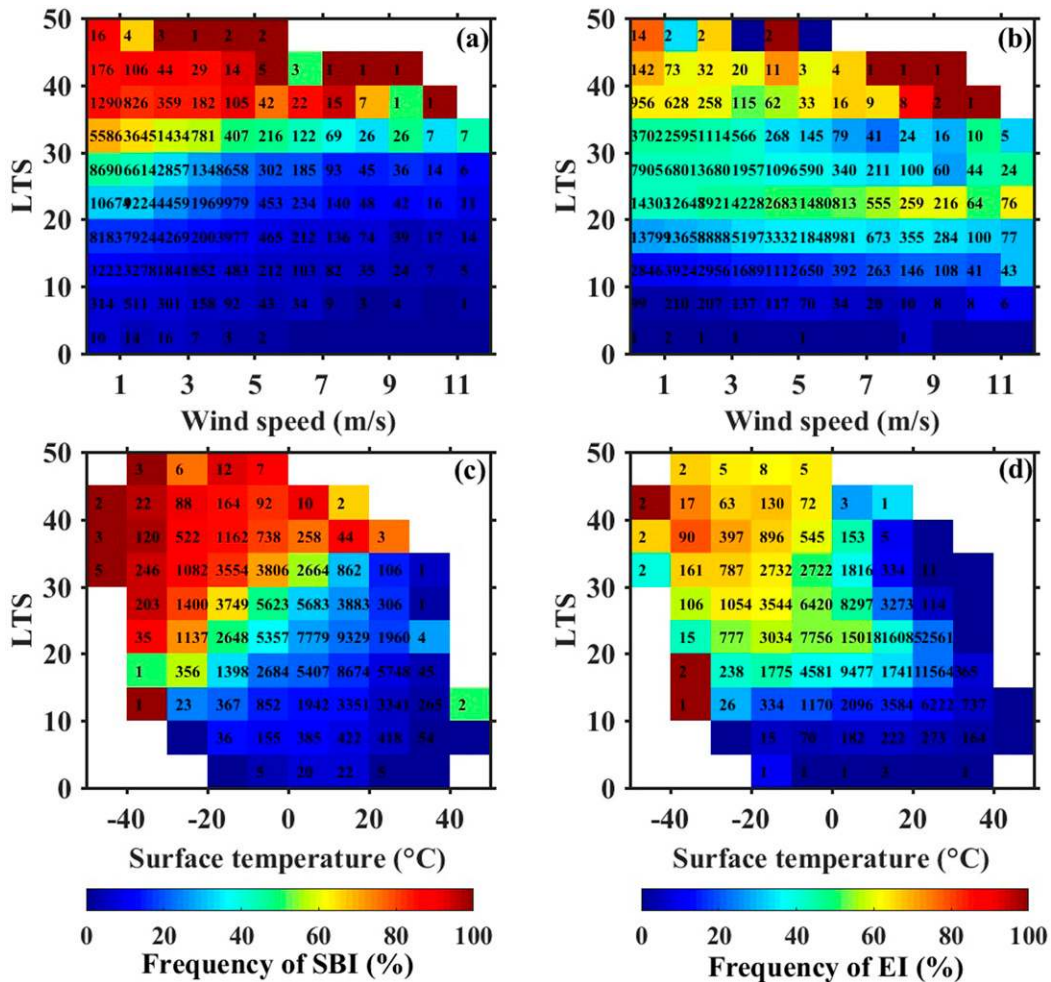
FIG. 22. Joint dependence of (a),(c) SBI and (b),(d) EI frequencies on 10-m wind speed, surface temperature, and lower troposphere stability (LTS; higher LTS denotes more stable PBL). Note that the number labeled in each cell represents its corresponding sample size.

study, we statistically present the climatological features of TIs in the PBL for the period 2011–17, including the occurrence frequency, depth, and intensity of SBI and EI, based on the 7-yr record of high-resolution upper-air sounding measurements from the China Radiosonde Network.

In general, the TI frequency exhibits a large geographic dependence. There is at least a 50% chance for almost the entire northwestern China to experience an SBI episode at 0800 BJT, which is much greater than over eastern China. The time lag of 1–2 h between BJT and LST leads to a typical nocturnal PBL in most sites of western China at the launch of soundings, which would result in negative latent and sensible heat fluxes associated with cooling ground and condensing water vapor. As a result, a positive gradient in temperature and specific humidity occurs, thereby facilitating the formation of SBI in western China. This primarily accounts for the "west high, east low" pattern. At 2000 BJT, the spatial pattern switches. In comparison, the spatial distribution of the EI frequency is much more uniform, with a relatively large frequency

in East China in both the morning and evening. Similarly, the depths for both SBIs and EIs do not exhibit a significant geographic dependence, although the SBI is much deeper in the morning than in the early evening. Additionally, the EI intensity is smaller than the SBI intensity, irrespective of in the morning or evening.

Both SBI and EI tend to occur more frequently at 0800 BJT, most likely owing to the stronger radiative cooling at 0800 BJT than at 2000 BJT. In particular, the summertime inversion frequency for both SBI and EI exhibits a pronounced diurnal variability, with a peak at 0800 BJT and a minimum at 1400 BJT. In the vertical direction, the largest EI frequency at 0800 BJT is observed at a height of approximately 300 m, except in winter, whereas the EI frequency at 2000 BJT reaches a maximum at heights between 1 and 2 km, except during summer. The highest SBI frequency usually occurs in winter, whereas the summer has the lowest frequency. Besides, the EI is found to occur most frequently in winter over Southeast China, which could be linked to both subsidence inversions and the heating
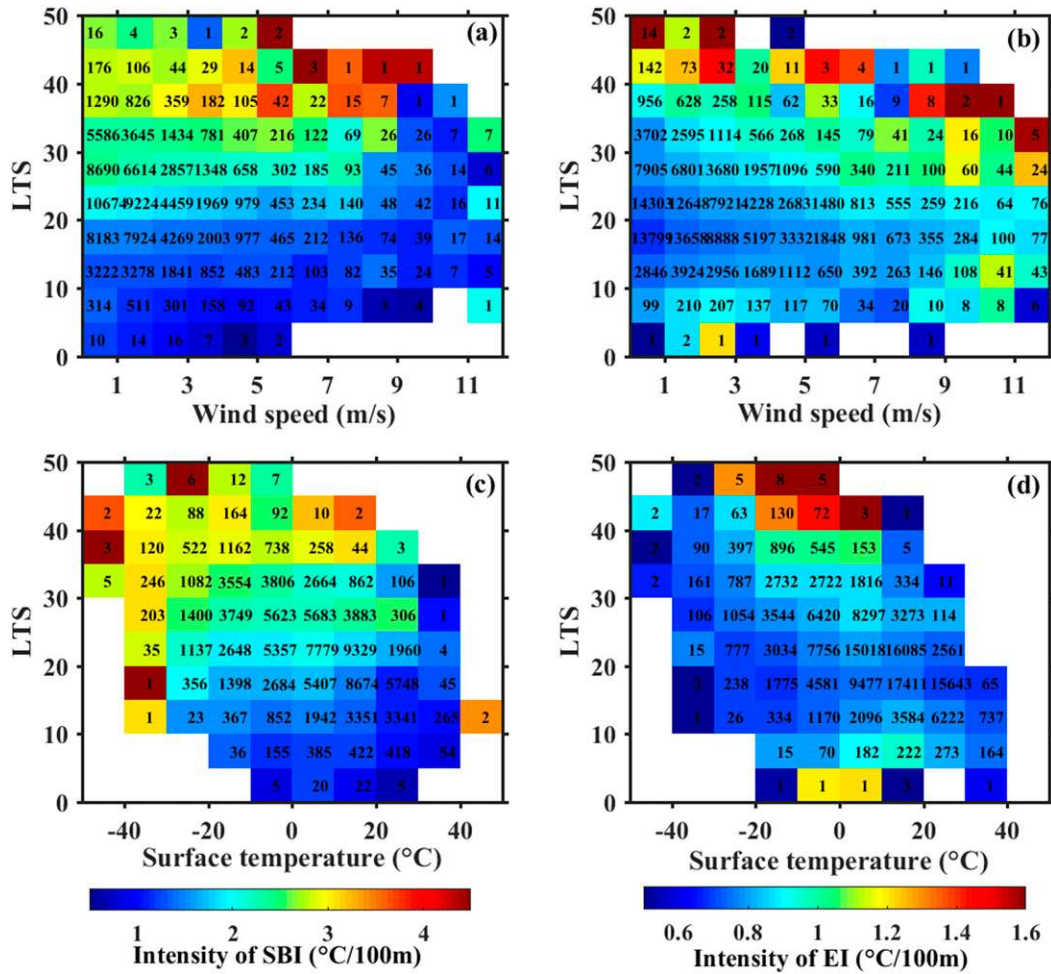
FIG. 23. As in Fig. 22, but for inversion intensity.

effect. The latter may be largely induced by the BC originating from the NCP. Besides, the role of trade inversion cannot be ignored either. Due to the strong variations in the loading and vertical distribution of BC, it remains a great challenging task to quantitatively confirm the heating effect of BC on EI based on observational analyses alone, which merits more observational and modeling studies in the future. Furthermore, it is hard to see any pronounced impact of topography and land cover on the seasonal and spatial patterns of TIs in China.

The relationships are analyzed between TIs and three local meteorological variables: surface temperature, 10-m wind speed, and LTS. The large wind speed and high surface temperature are linked to a lower SBI intensity, whereas a large LTS tends to be associated with a more intense SBI. In contrast, the EI intensity does not have a spatially uniform positive or negative correlation with any single meteorological variable across China, suggesting a combined effect of meteorological variables on the EI intensity. Furthermore, correlation analyses show that a greater LTS generally comes with a higher frequency of inversions and a stronger inversion intensity,

especially when the wind speed is weak, and the surface temperature is low. Conversely, when the LTS is small (unstable lower atmosphere), the wind speed and the surface temperature have little influence on the SBI or the EI frequency, indicating that the role of the above-mentioned surface meteorological variables can be ignored in regulating inversions under unstable PBL conditions. By comparison, the SBI intensity is found to be more dependent on the surface temperature than the EI intensity, whereas the dependence of EI intensity on local meteorology merely exists under restricted conditions.

The methods developed here to estimate TIs from high-resolution radiosonde measurements could be applied to other regions or countries. To the best of our knowledge, this is the first attempt to elucidate the climatological features of temperature inversions in the PBL across China using high-resolution radiosonde measurements. The classification of SBI and EI provides us deeper insight into the finer PBL structures over China. More importantly, the climatological dataset of TI would contribute to our understanding of the formation mechanisms of haze pollution and severe weather.

REFERENCES

Abdul-Wahab, S. A., S. Y. Al-Saifi, B. A. Alrumhi, M. Y. Abdulraheem, and M. Al-Uraimi, 2004: Determination of the features of the low-level temperature inversions above a suburban site in Oman using radiosonde temperature measurements: Long-term analysis. *J. Geophys. Res.*, **109**, D20101, https://doi.org/10.1029/2004JD004543.

André, J. C., and L. Mahrt, 1982: The nocturnal surface inversion and influence of clear-air radiative cooling. *J. Atmos. Sci.*, **39**, 864–878, https://doi.org/10.1175/1520-0469(1982)039<0864: TNSIAI>2.0.CO;2.

Anquetin, S., C. Guilbaud, and J.-P. Chollet, 1998: The formation and destruction of inversion layers within a deep valley. *J. Appl. Meteor.*, **37**, 1547–1560, https://doi.org/10.1175/1520-0450(1998)037<1547:TFADOI>2.0.CO;2.

Bailey, A., T. N. Chase, J. J. Cassano, and D. Noone, 2011: Changing temperature inversion characteristics in the U.S. Southwest and relationships to large-scale atmospheric circulation. *J. Appl. Meteor. Climatol.*, **50**, 1307–1323, https://doi.org/10.1175/2011JAMC2584.1.

Ball, F., 1960: Control of inversion height by surface heating. *Quart. J. Roy. Meteor. Soc.*, **86**, 483–494, https://doi.org/10.1002/qj.49708637005.

Beard, J. D., C. Beck, R. Graham, S. C. Packham, M. Traphagan, R. T. Giles, and J. G. Morgan, 2012: Winter temperature inversions and emergency department visits for asthma in Salt Lake County, Utah, 2003–2008. *Environ. Health Perspect.*, **120**, 1385–1390, https://doi.org/10.1289/ehp.1104349.

Bian, J., H. Chen, H. Vömel, Y. Duan, Y. Xuan, and D. Lü, 2011: Intercomparison of humidity and temperature sensors: GTS1, Vaisala RS80, and CFH. *Adv. Atmos. Sci.*, **28**, 139–146, https://doi.org/10.1007/s00376-010-9170-8.

Boucher, O., and Coauthors, 2013: Clouds and aerosols. *Climate Change 2013: The Physical Science Basis*, T. F. Stocker et al., Eds., Cambridge University Press, 571–657.

Buchard, V., and Coauthors, 2017: The MERRA-2 aerosol reanalysis, 1980 onward. Part II: Evaluation and case studies. *J. Climate*, **30**, 6851–6872, https://doi.org/10.1175/JCLI-D-16-0613.1.

Cao, G., X. Zhang, and F. Zheng, 2006: Inventory of black carbon and organic carbon emissions from China. *Atmos. Environ.*, **40**, 6516–6527, https://doi.org/10.1016/j.atmosenv.2006.05.070.

Cao, J. J., C. S. Zhu, J. C. Chow, J. G. Watson, Y. M. Han, G. H. Wang, Z. X. Shen, and Z. S. An, 2009: Black carbon relationships with emissions and meteorology in Xi'an, China. *Atmos. Res.*, **94**, 194–202, https://doi.org/10.1016/j.atmosres.2009.05.009.

Cassano, J. J., M. A. Nigro, and M. A. Lazzara, 2016: Characteristics of the near-surface atmosphere over the Ross Ice Shelf, Antarctica. *J. Geophys. Res. Atmos.*, **121**, 3339–3362, https://doi.org/10.1002/2015JD024383.

Chen, D., J. Guo, H. Wang, J. Li, M. Min, W. Zhao, and D. Yao, 2018: The cloud top distribution and diurnal variation of clouds over East Asia: Preliminary results from Advanced Himawari Imager. *J. Geophys. Res. Atmos.*, **123**, 3724–3739, https://doi.org/10.1002/2017JD028044.

Chen, S., J. Guo, L. Song, J. Cohen, and Y. Wang, 2020: Temporal disparity of the atmospheric systems contributing to interannual variation of wintertime haze pollution in the North China Plain. *Int. J. Climatol.*, **40**, 128–144, https://doi.org/10.1002/joc.6198.

Chen, W., H. F. Graf, and R. Huang, 2000: The interannual variability of East Asian winter monsoon and its relation to the summer monsoon. *Adv. Atmos. Sci.*, **17**, 48–60, https://doi.org/10.1007/s00376-000-0042-5.

Chen, Y. L., and J. Feng, 1995: The influences of inversion height on precipitation and airflow over the island of Hawaii. *Mon. Wea. Rev.*, **123**, 1660–1676, https://doi.org/10.1175/1520-0493(1995)123<1660:TIOIHO>2.0.CO;2.

——, and ——, 2001: Numerical simulations of airflow and cloud distributions over the windward side of the island of Hawaii. Part I: The effects of trade wind inversion. *Mon. Wea. Rev.*, **129**, 1117–1134, https://doi.org/10.1175/1520-0493(2001)129<1117: NSOAAC>2.0.CO;2.

Cheng, C. S., and Coauthors, 2007: A synoptic climatological approach to assess climatic impact on air quality in south-central Canada. Part I: Historical analysis. *Water Air Soil Pollut.*, **182**, 131–148, https://doi.org/10.1007/s11270-006-9327-3.

Connolley, W. M., 1996: The Antarctic temperature inversion. *Int. J. Climatol.*, **16**, 1333–1342, https://doi.org/10.1002/(SICI)1097-0088(199612)16:12<1333::AID-JOC96>3.0.CO;2-6.

Coy, L., K. Wargan, A. M. Molod, W. R. McCarty, and S. Pawson, 2016: Structure and dynamics of the quasi-biennial oscillation in MERRA-2. *J. Climate*, **29**, 5339–5354, https://doi.org/10.1175/JCLI-D-15-0809.1.

Deser, C., R. Tomas, M. Alexander, and D. Lawrence, 2010: The seasonal atmospheric response to projected Arctic sea ice loss in the late twenty-first century. *J. Climate*, **23**, 333–351, https://doi.org/10.1175/2009JCLI3053.1.

Devasthale, A., U. Willén, K. G. Karlsson, and C. G. Jones, 2010: Quantifying the clear-sky temperature inversion frequency and strength over the Arctic Ocean during summer and winter seasons from AIRS profiles. *Atmos. Chem. Phys.*, **10**, 5565–5572, https://doi.org/10.5194/acp-10-5565-2010.

Ding, A. J., and Coauthors, 2016: Enhanced haze pollution by black carbon in megacities in China. *Geophys. Res. Lett.*, **43**, 2873–2879, https://doi.org/10.1002/2016GL067745.

Ding, Y., 1994: *Monsoons over China*. Springer, 419 pp.

Fast, J. D., S. Zhong, and C. D. Whiteman, 1996: Boundary layer evolution within a canyonland basin. Part II: Numerical simulations of nocturnal flows and heat budgets. *J. Appl. Meteor.*, **35**, 2162–2178, https://doi.org/10.1175/1520-0450(1996)035<2162:BLEWAC>2.0.CO;2.

Ferrero, L., and Coauthors, 2014: Impact of black carbon aerosol over Italian basin valleys: High-resolution measurements along vertical profiles, radiative forcing and heating rate. *Atmos. Chem. Phys.*, **14**, 9641–9664, https://doi.org/10.5194/acp-14-9641-2014.

Garreaud, R., and R. C. Muñoz, 2005: The low-level jet off the west coast of subtropical South America: Structure and variability. *Mon. Wea. Rev.*, **133**, 2246–2261, https://doi.org/10.1175/MWR2971.1.

Gelaro, R., and Coauthors, 2017: The Modern-Era Retrospective Analysis for Research and Applications, version 2 (MERRA-2). *J. Climate*, **30**, 5419–5454, https://doi.org/10.1175/JCLI-D-16-0758.1.

Gramsch, E., D. Caceres, P. Oyola, E. Reyes, Y. Vasquez, M. A. Rubio, and G. Sanchez, 2014: Influence of surface and subsidence thermal inversion on $PM_{2.5}$ and black carbon concentration. *Atmos. Environ.*, **98**, 290–298, https://doi.org/10.1016/j.atmosenv.2014.08.066.

Guo, J., X.-Y. Zhang, Y.-R. Wu, Y. Zhaxi, H.-Z. Che, B. La, W. Wang, and X.-W. Li, 2011: Spatio-temporal variation trends of satellite-based aerosol optical depth in China during 1980–2008. *Atmos. Environ.*, **45**, 6802–6811, https://doi.org/10.1016/j.atmosenv.2011.03.068.

——, and Coauthors, 2016a: Delaying precipitation and lightning by air pollution over the Pearl River Delta. Part I: Observational analyses. *J. Geophys. Res. Atmos.*, **121**, 6472–6488, https://doi.org/10.1002/2015JD023257.

——, and Coauthors, 2016b: The climatology of planetary boundary layer height in China derived from radiosonde and reanalysis data. *Atmos. Chem. Phys.*, **16**, 13 309–13 319, https://doi.org/10.5194/acp-16-13309-2016.

——, and Coauthors, 2017: Impact of diurnal variability and meteorological factors on the $PM_{2.5}$–AOD relationship: Implications for $PM_{2.5}$ remote sensing. *Environ. Polit.*, **221**, 94–104, https://doi.org/10.1016/j.envpol.2016.11.043.

——, and Coauthors, 2018: Aerosol-induced changes in the vertical structure of precipitation: A perspective of TRMM precipitation radar. *Atmos. Chem. Phys.*, **18**, 13 329–13 343, https://doi.org/10.5194/acp-18-13329-2018.

——, and Coauthors, 2019: Shift in the temporal trend of boundary layer height trend in China using long-term (1979–2016) radiosonde data. *Geophys. Res. Lett.*, **46**, 6080–6089, https://doi.org/10.1029/2019GL082666.

Holzworth, G. C., 1972: Vertical temperature structure during the 1966 Thanksgiving week air pollution episode in New York City. *Mon. Wea. Rev.*, **100**, 445–450, https://doi.org/10.1175/1520-0493(1972)100<0445:VTSDTT>2.3.CO;2.

Huang, X., Z. Wang, and A. Ding, 2018: Impact of aerosol–PBL interaction on haze pollution: Multiyear observational evidences in North China. *Geophys. Res. Lett.*, **45**, 8596–8603, https://doi.org/10.1029/2018GL079239.

Hyun, Y.-K., K.-E. Kim, and K.-J. Ha, 2005: A comparison of methods to estimate the height of stable boundary layer over a temperate grassland. *Agric. For. Meteor.*, **132**, 132–142, https://doi.org/10.1016/j.agrformet.2005.03.010.

Janhall, S., K. Olofson, P. Andersson, J. Pettersson, and M. Hallquist, 2006: Evolution of the urban aerosol during winter temperature inversion episodes. *Atmos. Environ.*, **40**, 5355–5366, https://doi.org/10.1016/j.atmosenv.2006.04.051.

Ji, F., and Coauthors, 2018: Projected change in characteristics of near surface temperature inversions for southeast Australia. *Climate Dyn.*, **52**, 1487–1503, https://doi.org/10.1007/s00382-018-4214-3.

Johnson, R. H., P. E. Ciesielski, and K. A. Hart, 1996: Tropical inversions near the 0°C level. *J. Atmos. Sci.*, **53**, 1838–1855, https://doi.org/10.1175/1520-0469(1996)053<1838:TINTL>2.0.CO;2.

Kahl, J. D., 1990: Characteristics of the low-level temperature inversion along the Alaskan Arctic coast. *Int. J. Climatol.*, **10**, 537–548, https://doi.org/10.1002/joc.3370100509.

Kassomenos, P. A., A. K. Paschalidou, S. Lykoudis, and I. Koletsis, 2014: Temperature inversion characteristics in relation to synoptic circulation above Athens, Greece. *Environ. Monit. Assess.*, **186**, 3495–3502, https://doi.org/10.1007/s10661-014-3632-x.

Kay, J. E., and A. Gettelman, 2009: Cloud influence on and response to seasonal Arctic Sea ice loss. *J. Geophys. Res.*, **114**, D18204, https://doi.org/10.1029/2009JD011773.

Kukkonen, J., and Coauthors, 2005: Analysis and evaluation of selected local-scale PM_{10} air pollution episodes in four European cities: Helsinki, London, Milan and Oslo. *Atmos. Environ.*, **39**, 2759–2773, https://doi.org/10.1016/j.atmosenv.2004.09.090.

Li, J., H. Chen, Z. Li, P. Wang, M. Cribb, and X. Fan, 2015: Low-level temperature inversions and their effect on aerosol condensation nuclei concentrations under different large-scale synoptic circulations. *Adv. Atmos. Sci.*, **32**, 898–908, https://doi.org/10.1007/s00376-014-4150-z.

Li, Z., and Coauthors, 2016: Aerosol and monsoon climate interactions over Asia. *Rev. Geophys.*, **54**, 866–929, https://doi.org/10.1002/2015RG000500.

——, and Coauthors, 2017: Aerosol and boundary-layer interactions and impact on air quality. *Natl. Sci. Rev.*, **4**, 810–833, https://doi.org/10.1093/nsr/nwx117.

Lilly, D. K., 1968: Models of cloud-topped mixed layers under a strong inversion. *Quart. J. Roy. Meteor. Soc.*, **94**, 292–309, https://doi.org/10.1002/qj.49709440106.

Liu, L., J. Guo, Y. Miao, J. Li, D. Chen, J. He, and C. Cui, 2018: Elucidating the relationship between aerosol concentration and summertime boundary layer structure in central China. *Environ. Pollut.*, **241**, 646–653, https://doi.org/10.1016/j.envpol.2018.06.008.

Liu, Y., and J. R. Key, 2003: Detection and analysis of clear-sky, low-level atmospheric temperature inversions with MODIS. *J. Atmos. Oceanic Technol.*, **20**, 1727–1737, https://doi.org/10.1175/1520-0426(2003)020<1727:DAAOCL>2.0.CO;2.

Lüpkes, C., T. Vihma, G. Birnbaum, and U. Wacker, 2008: Influence of leads in sea ice on the temperature of the atmospheric boundary layer during polar night. *Geophys. Res. Lett.*, **35**, L03805, https://doi.org/10.1029/2007GL032461.

Ma, Y., W. Yao, and B. Huang, 2011: Comparison of temperature and geopotential height records between 59 type and L-band radiosonde systems. *J. Appl. Meteor. Sci.*, **22**, 336–345.

Mernild, S. H., and G. E. Liston, 2010: The influence of air temperature inversions on snowmelt and glacier mass balance simulations, Ammassalik Island, southeast Greenland. *J. Appl. Meteor. Climatol.*, **49**, 47–67, https://doi.org/10.1175/2009JAMC2065.1.

Miao, Y., J. Guo, S. Liu, H. Liu, Z. Li, W. Zhang, and P. Zhai, 2017a: Classification of summertime synoptic patterns in Beijing and their association with boundary layer structure affecting aerosol pollution. *Atmos. Chem. Phys.*, **17**, 3097–3110, https://doi.org/10.5194/acp-17-3097-2017.

——, ——, ——, ——, G. Zhang, Y. Yan, and J. He, 2017b: Relay transport of aerosols to Beijing-Tianjin-Hebei region by multiscale atmospheric circulations. *Atmos. Environ.*, **165**, 35–45, https://doi.org/10.1016/j.atmosenv.2017.06.032.

Milionis, A. E., and T. D. Davies, 2008: The effect of the prevailing weather on the statistics of atmospheric temperature inversions. *Int. J. Climatol.*, **28**, 1385–1397, https://doi.org/10.1002/joc.1613.

Nodzu, M. I., S.-Y. Ogino, Y. Tachibana, and M. D. Yamanaka, 2006: Climatological description of seasonal variations in lower-tropospheric temperature inversion layers over the Indochina Peninsula. *J. Climate*, **19**, 3307–3319, https://doi.org/10.1175/JCLI3792.1.

Nygård, T., P. Tisler, T. Vihma, R. Pirazzini, T. Palo, and R. Kouznetsov, 2017: Properties and temporal variability of

summertime temperature inversions over Dronning Maud Land, Antarctica. *Quart. J. Roy. Meteor. Soc.*, **143**, 582–595, https://doi.org/10.1002/qj.2951.

Olofson, K. F. G., P. U. Andersson, M. Hallquist, E. Ljungström, L. Tang, D. Chen, and J. B. Pettersson, 2009: Urban aerosol evolution and particle formation during wintertime temperature inversions. *Atmos. Environ.*, **43**, 340–346, https://doi.org/10.1016/j.atmosenv.2008.09.080.

Palarz, A., D. Celiński-Mysław, and Z. Ustrnul, 2018: Temporal and spatial variability of surface-based inversions over Europe based on ERA-Interim reanalysis. *Int. J. Climatol.*, **38**, 158–168, https://doi.org/10.1002/joc.5167.

Pavelsky, T. M., J. Boé, A. Hall, and E. J. Fetzer, 2011: Atmospheric inversion strength over polar oceans in winter regulated by sea ice. *Climate Dyn.*, **36**, 945–955, https://doi.org/10.1007/s00382-010-0756-8.

Petty, G. W., 2006: *A First Course in Atmospheric Radiation*. 2nd ed. Sundog Publishing, 459 pp.

Qian, Y., L. R. Leung, S. J. Ghan, and F. Giorgi, 2011: Regional climate effects of aerosols over China: Modeling and observation. *Tellus*, **55B**, 914–934, https://doi.org/10.3402/tellusb.v55i4.16379.

Rendón, A. M., J. F. Salazar, C. A. Palacio, V. Wirth, and B. Brötz, 2014: Effects of urbanization on the temperature inversion breakup in a mountain valley with implications for air quality. *J. Appl. Meteor. Climatol.*, **53**, 840–858, https://doi.org/10.1175/JAMC-D-13-0165.1.

Rienecker, M. M., and Coauthors, 2011: MERRA: NASA's Modern-Era Retrospective Analysis for Research and Applications. *J. Climate*, **24**, 3624–3648, https://doi.org/10.1175/JCLI-D-11-00015.1.

Riordan, A. J., 1977: Variations of temperature and air motion in the 0- to 32-meter layer at Plateau Station, Antarctica. *Meteorological Studies at Plateau Station, Antarctica*, P. C. Dalrymple et al., Eds., Antarctic Research Series, Vol. 25, Amer. Geophys. Union, 113–127.

Seidel, D. J., Y. Zhang, A. Beljaars, J. C. Golaz, A. R. Jacobson, and B. Medeiros, 2012: Climatology of the planetary boundary layer over the continental United States and Europe. *J. Geophys. Res.*, **117**, D17106, https://doi.org/10.1029/2012JD018143.

Serreze, M. C., R. C. Schnell, and J. D. Kahl, 1992: Low-level temperature inversions of the Eurasian Arctic and comparisons with Soviet drifting station data. *J. Climate*, **5**, 615–629, https://doi.org/10.1175/1520-0442(1992)005<0615:LLTIOT>2.0.CO;2.

Slingo, J., 1987: The development and verification of a cloud prediction scheme for the ECMWF model. *Quart. J. Roy. Meteor. Soc.*, **113**, 899–927, https://doi.org/10.1002/qj.49711347710.

Steeneveld, G. J., M. J. J. Wokke, C. D. Groot Zwaaftink, S. Pijlman, B. G. Heusinkveld, A. F. G. Jacobs, and A. A. M. Holtslag, 2010: Observations of the radiation divergence in the surface layer and its implication for its parameterization in numerical weather prediction models. *J. Geophys. Res.*, **115**, D06107, https://doi.org/10.1029/2009JD013074.

Stevens, B., 2002: Entrainment in stratocumulus-topped mixed layers. *Quart. J. Roy. Meteor. Soc.*, **128**, 2663–2690, https://doi.org/10.1256/qj.01.202.

——, 2007: On the growth of layers of nonprecipitating cumulus convection. *J. Atmos. Sci.*, **64**, 2916–2931, https://doi.org/10.1175/JAS3983.1.

——, and Coauthors, 2003: On entrainment rates in nocturnal marine stratocumulus. *Quart. J. Roy. Meteor. Soc.*, **129**, 3469–3493, https://doi.org/10.1256/qj.02.202.

Stull, R. B., 1988: *An Introduction to Boundary Layer Meteorology*. Kluwer Academic, 666 pp.

Su, T., J. Li, C. Li, P. Xiang, A. K. H. Lau, J. Guo, D. Yang, and Y. Miao, 2017: An intercomparison of long-term planetary boundary layer heights retrieved from CALIPSO, ground-based lidar, and radiosonde measurements over Hong Kong. *J. Geophys. Res. Atmos.*, **122**, 3929–3943, https://doi.org/10.1002/2016JD025937.

——, Z. Li, and R. Kahn, 2018: Relationships between the planetary boundary layer height and surface pollutants derived from lidar observations over China: Regional pattern and influencing factors. *Atmos. Chem. Phys.*, **18**, 15 921–15 935, https://doi.org/10.5194/acp-18-15921-2018.

——, and Coauthors, 2020: The significant impact of aerosol vertical structure on lower atmosphere stability and its critical role in aerosol–planetary boundary layer (PBL) interactions. *Atmos. Chem. Phys.*, **20**, 3713–3724, https://doi.org/10.5194/acp-20-3713-2020.

Tao, S., X. Chen, and J. Gong, 2006: Error analyses for temperature of L band radiosonde. *Meteor. Monogr.*, **32**, 46–51.

Tomasi, C., 1977: Precipitable water vapor in atmospheres characterized by temperature inversions. *J. Appl. Meteor.*, **16**, 237–243, https://doi.org/10.1175/1520-0450(1977)016<0237:PWVIAC>2.0.CO;2.

Trompetter, W. J., S. K. Grange, P. K. Davy, and T. Ancelet, 2013: Vertical and temporal variations of black carbon in New Zealand urban areas during winter. *Atmos. Environ.*, **75**, 179–187, https://doi.org/10.1016/j.atmosenv.2013.04.036.

Vihma, T., T. Kilpeläinen, M. Manninen, A. Sjöblom, E. Jakobson, T. Palo, J. Jaagus, and M. Maturilli, 2011: Characteristics of temperature and humidity inversions and low-level jets over Svalbard fjords in spring. *Adv. Meteor.*, **2011**, 486807, https://doi.org/10.1155/2011/486807.

Wallace, J., and P. Kanaroglou, 2009a: The effect of temperature inversions on ground-level nitrogen dioxide (NO_2) and fine particulate matter ($PM_{2.5}$) using temperature profiles from the Atmospheric Infrared Sounder (AIRS). *Sci. Total Environ.*, **407**, 5085–5095, https://doi.org/10.1016/j.scitotenv.2009.05.050.

——, and ——, 2009b: The sensitivity of OMI-derived nitrogen dioxide to boundary layer temperature inversions. *Atmos. Environ.*, **43**, 3596–3604, https://doi.org/10.1016/j.atmosenv.2009.03.049.

Wang, H., J. Xu, M. Zhang, Y. Yang, X. Shen, Y. Wang, D. Chen, and J. Guo, 2014: A study of the meteorological causes of a prolonged and severe haze episode in January 2013 over central-eastern China. *Atmos. Environ.*, **98**, 146–157, https://doi.org/10.1016/j.atmosenv.2014.08.053.

Wang, Q., and Coauthors, 2020: Interannual variability of South China Sea winter circulation: Response to Luzon Strait transport and El Niño wind. *Climate Dyn.*, **54**, 1145–1159, https://doi.org/10.1007/s00382-019-05050-2.

Wang, Y. J., and Coauthors, 2016: Analysis of land surface parameters and turbulence characteristics over the Tibetan Plateau and surrounding region. *J. Geophys. Res. Atmos.*, **121**, 9540–9560, https://doi.org/10.1002/2016JD025401.

Wang, Z., X. Huang, and A. Ding, 2018: Dome effect of black carbon and its key influencing factors: A one-dimensional modeling study. *Atmos. Chem. Phys.*, **18**, 2821–2834, https://doi.org/10.5194/acp-18-2821-2018.

Wehner, B., and A. Wiedensohler, 2003: Long term measurements of submicrometer urban aerosols: Statistical analysis for correlations with meteorological conditions and trace gases. *Atmos. Chem. Phys.*, **3**, 867–879, https://doi.org/10.5194/acp-3-867-2003.

Whiteman, C. D., T. B. McKee, and J. Doran, 1996: Boundary layer evolution within a canyonland basin. Part I: Mass, heat, and moisture budgets from observations. *J. Appl. Meteor.*, **35**, 2145–2161, https://doi.org/10.1175/1520-0450(1996)035<2145:BLEWAC>2.0.CO;2.

——, X. Bian, and S. Zhong, 1999: Wintertime evolution of the temperature inversion in the Colorado plateau basin. *J. Appl. Meteor.*, **38**, 1103–1117, https://doi.org/10.1175/1520-0450(1999)038<1103:WEOTTI>2.0.CO;2.

Xiao, Q., Z. Ma, S. Li, and Y. Liu, 2015: The impact of winter heating on air pollution in China. *PLOS ONE*, **10**, e0117311, https://doi.org/10.1371/journal.pone.0117311.

Xu, T., Y. Song, M. Liu, X. Cai, H. Zhang, J. Guo, and T. Zhu, 2019: Temperature inversions in severe polluted days derived from radiosonde data in North China from 2011 to 2016. *Sci. Total Environ.*, **647**, 1011–1020, https://doi.org/10.1016/j.scitotenv.2018.08.088.

Yan, Y., and Coauthors, 2019: Synoptic patterns and sounding-derived parameters associated with summertime heavy rainfall in Beijing. *Int. J. Climatol.*, **39**, 1476–1489, https://doi.org/10.1002/joc.5895.

Yang, Y., X. Zheng, Z. Gao, H. Wang, T. Wang, Y. Li, G. N. C. Lau, and S. H. L. Yim, 2018: Long-term trends of persistent synoptic circulation events in planetary boundary layer and their relationships with haze pollution in winter half-year over eastern China. *J. Geophys. Res. Atmos.*, **123**, 10 991–11 007, https://doi.org/10.1029/2018JD028982.

Yin, P., and Coauthors, 2020: Higher risk of cardiovascular disease associated with smaller size-fractioned particulate matter. *Environ. Sci. Technol. Lett.*, **7**, 95–101, https://doi.org/10.1021/acs.estlett.9b00735.

Zhang, Q., X. Ma, X. Tie, M. Huang, and C. Zhao, 2009: Vertical distributions of aerosols under different weather conditions: Analysis of in-situ aircraft measurements in Beijing, China. *Atmos. Environ.*, **43**, 5526–5535, https://doi.org/10.1016/j.atmosenv.2009.05.037.

Zhang, R.-H., S. Zhang, J. Luo, Y. Han, and J. Zhang, 2019: Analysis of near-surface wind speed change in China during 1958–2015. *Theor. Appl. Climatol.*, **137**, 2785–2801, https://doi.org/10.1007/s00704-019-02769-0.

Zhang, W., J. Guo, Y. Miao, H. Liu, Y. Zhang, Z. Li, and P. Zhai, 2016: Planetary boundary layer height from CALIOP compared to radiosonde over China. *Atmos. Chem. Phys.*, **16**, 9951–9963, https://doi.org/10.5194/acp-16-9951-2016.

——, and Coauthors, 2018: On the summertime planetary boundary layer with different thermodynamic stability in China: A radiosonde perspective. *J. Climate*, **31**, 1451–1465, https://doi.org/10.1175/JCLI-D-17-0231.1.

Zhang, Y., and Coauthors, 2018: Climatology of cloud-base height from long-term radiosonde measurements in China. *Adv. Atmos. Sci.*, **35**, 158–168, https://doi.org/10.1007/s00376-017-7096-0.

——, Y. Li, J. Guo, Y. Wang, D. Chen, and H. Chen, 2019: The climatology and trend of black carbon in China from 12-year ground observations. *Climate Dyn.*, **53**, 5881–5892, https://doi.org/10.1007/s00382-019-04903-0.

Zhao, D., and Coauthors, 2020: Vertical evolution of black carbon characteristics and heating rate during a haze event in Beijing winter. *Sci. Total Environ.*, **709**, 136251, https://doi.org/10.1016/j.scitotenv.2019.136251.

Zheng, Y., D. Rosenfeld, Y. Zhu, and Z. Li, 2019: Satellite-based estimation of cloud top radiative cooling rate for marine stratocumulus. *Geophys. Res. Lett.*, **46**, 4485–4494, https://doi.org/10.1029/2019GL082094.